Astral microtubule crosslinking by Feo safeguards uniform nuclear distribution in the *Drosophila* syncytium

Ojas Deshpande[*], Jorge de-Carvalho[*,#], Diana V. Vieira[*,#] and Ivo A. Telley[*,§]

[*] Instituto Gulbenkian de Ciência, Fundação Calouste Gulbenkian, Oeiras, Portugal

[#] Co-authors in alphabetical order

[§] Lead contact

Correspondence to: itelley@igc.gulbenkian.pt

Keywords: PRC1, Kif4, coenocyte, central spindle, microtubule interaction, nuclear positioning

Abstract:

The early insect embryo develops as multinucleated cell distributing genomes uniformly to the cell cortex. Mechanistic insight for nuclear positioning beyond cytoskeletal requirements is missing to date. Contemporary hypotheses propose actomyosin driven cytoplasmic movement transporting nuclei, or repulsion of neighbor nuclei driven by microtubule motors. Here, we show that microtubule crosslinking by Feo and Klp3A is essential for nuclear distribution and internuclear distance maintenance in *Drosophila*. RNAi knockdown in the germline causes irregular, less dense nuclear delivery to the embryo cortex and smaller distribution in *ex vivo* embryo explants. A minimal internuclear distance is maintained in explants from control embryos but not from Feo depleted embryos, following micromanipulation assisted repositioning. A dominant-negative Feo protein abolishes nuclear separation in embryo explants while the full-length protein rescues the genetic knockdown. We conclude that antiparallel microtubule overlap crosslinking by Feo and Klp3A generates a length-regulated mechanical link between neighboring microtubule asters. Enabled by a novel experimental approach, our study illuminates an essential process of embryonic multicellularity.

Introduction

The nucleus relocates within the cell boundary in response to cell function[1,2]. Aberrant nuclear positioning has been linked to failure of fundamental processes such as early embryo development, cell differentiation, cell migration, polarity determination and homeostasis[3-8]. Nuclear positioning depends on a set of nuclear envelope proteins linking the cytoskeletal network and transmitting active force generation to the nucleus for movement[1,9]. In mononuclear cells, cytoskeletal elements mechanically connect the nucleus to the cell cortex being the reference system for positioning[10,11]. One exception are large eggs in which cytoskeletal links between the nucleus and the distant cell cortex are not achieved[12]. Conversely, a multinucleated cell – coenocyte – undergoing nuclear proliferation has to generate positional information with each additional nucleus and requires a mechanism that adjusts the distance between neighboring nuclei[13]. The early embryo of *Drosophila melanogaster* is both large and multinucleated but exhibits a surprising positional regularity of hundreds of nuclei perturbed by rounds of meta-synchronous nuclear divisions [14]. During the first seven rounds, the nuclei spread axially from the anterior to the posterior end of the embryo and occupy the entire cell volume[15]. During nuclear cycles 7–9, most nuclei migrate to the embryo cortex, where they undergo additional rounds of division as they are anchored and prepared for cellularization[16]. Adequate number of nuclei and their proper positioning at the cortex determines cell size[17], is essential for epithelia formation and subsequent development[18,19] and is a result of regular distribution of ancestor nuclei during the preceding developmental phase[20-22]. The mechanisms required for maintaining the internuclear distances uniformly are not understood. Drug inhibition and mutagenesis suggest that actomyosin mediated cortical contractions drive cytoplasmic streaming and transport the nuclei predominantly along the longer axis of the embryo[17,23-27]. However, large-scale transport of cytoplasm does neither explain how a uniform distribution emerges nor how nuclei are kept separate. Conversely, astral microtubules are required for nuclear movement[28], and embryos with abnormal microtubule aster morphology exhibit nuclear collision or spindle fusion[20-22]. Baker et al.[15] proposed a repulsion mechanism by motor binding and sliding antiparallel overlaps of astral microtubules from neighboring nuclei, which is reminiscent of the spindle midzone model explaining spindle elongation during anaphase B[29,30]. At the core lies Klp61F, a homotetrameric, bipolar Kinesin-5 which binds two overlapping microtubules and, when microtubules are antiparallel, slides them outwards reducing microtubule overlap length[31-33]. Fascetto (Feo) is the *Drosophila* homolog of the Ase1p/PRC1/MAP65 family of homodimeric, non-motor microtubule-associated proteins (MAPs) which preferentially binds antiparallel microtubule overlaps[34-36]. It accumulates at the spindle midzone from anaphase to telophase upon cyclin B degradation and controls the binding affinity of molecular motors in the

63 spindle midzone[29,37-40]. One of these motors is Klp3A, a Kinesin-4 homolog, a microtubule
64 depolymerase with chromatin binding affinity[35,41-44]. PRC1 and Kinesin-4 are sufficient to form a
65 stable microtubule overlap *in vitro*[35]. Kinesin-5 is able to reduce overlapping, antiparallel
66 microtubules crosslinked by PRC1 *in vitro*[36], which was proposed to contribute to force balance in
67 the spindle midzone during anaphase B[30]. Here, we investigated whether these three proteins are
68 required for nuclear separation, lending support to an aster–aster interaction model[15,45]. We
69 performed a combination of gene knockdown, micromanipulation and perturbation by exogenous
70 protein addition in embryo explants which enable time-lapse visualization of nuclear and
71 cytoskeletal dynamics previously unachieved.

72 **Results**

73 ***Feo localization confirm antiparallel microtubule overlaps between asters of non-sister nuclei***

74 Molecular crosslinking between astral microtubules of neighboring nuclei during the
75 preblastoderm embryo stage has been largely unexplored due to optical constraints in live imaging.
76 Using an extraction method to generate cytoplasmic explants from individual preblastoderm
77 embryos[46] expressing Klp61F::GFP and Feo::mCherry, and injected with Alexa647-labeled
78 Tubulin (Fig. 1a), we visualized the localization of Klp61F and Feo to infer about their binding to
79 spindle microtubules (Fig. 1b). Klp61F::GFP localized at the microtubule-organizing centers
80 (MTOC), the metaphase spindle and the spindle midzone in anaphase, as described previously for
81 the nuclear divisions at the blastoderm stage[31,33,47-49] (Suppl. Video 1). Furthermore, during
82 anaphase B and telophase we observed Klp61F::GFP decorated microtubules intercalating with
83 those from the neighboring aster, raising the possibility of antiparallel alignment of these astral
84 microtubules, forming an overlap zone to which Kinesin-5 binds. On the other hand, Feo::mCherry
85 exhibited weak localization to the metaphase spindle but strong localization to the spindle midzone
86 during anaphase B and telophase (Fig. 1b, arrows), as previously described for blastoderm division
87 cycles[38]. Strikingly, Feo also localized in small foci to the region between the nuclei (Fig. 1b,c,
88 arrowheads), thus reporting the presence of antiparallel microtubule overlaps which Feo binds to
89 with higher affinity than individual microtubules. *In vitro*, microtubule overlaps that are decorated
90 by Feo homologs are length controlled through the polymerase activity of Kinesin-4[35]. Thus, the
91 signal of Feo along microtubule overlaps should have a consistent length for a given concentration
92 or activity of Feo and Klp3A. Thus, we measured the length of Feo::GFP signal foci during
93 anaphase B (Fig. 1d). Because individual microtubules were not resolved, we measured the
94 orientation of the signal foci in the context of where microtubules are growing and radially
95 emanating from, the MTOCs at the spindle pole. In anaphase and telophase, the four nuclei

96 emerging from any two neighboring spindles define four MTOCs and, thus, four possible
97 combinations of astral microtubules interacting (Fig. 1c, right). We measured the angle θ between
98 the long axes of the signal foci and the closest connecting line between two MTOCs (Fig. 1e). This
99 angle deviated little from zero, supporting the notion that Feo reports microtubule overlaps along
100 the shortest path between neighboring asters. Altogether, in extract from preblastoderm embryos,
101 the relative position of nuclei and the length of astral microtubules leads to the formation of short
102 antiparallel microtubule overlaps which Feo binds to. Furthermore, as a consequence of Feo
103 crosslinking astral microtubules, a mechanical connection is established that may be controlling
104 the distance between neighboring asters and their associated nuclei.

105 During the last four syncytial nuclear cycles at the cortex, the current understanding of nuclear
106 separation is thought to be embodied by the actin based pseudo-compartment driving membrane
107 invagination, a physical barrier that is assembled and disassembled in every division cycle[50,51].
108 Surprisingly, time-lapse confocal imaging of living embryos expressing either Klp61F::GFP and
109 Feo::mCherry (Fig. 1f, Suppl. Video 2) or Klp3A::GFP and Feo::mCherry (Fig. 1g, Suppl. Video
110 3), after injection of Alexa647–Tubulin, revealed strong localization at the spindle midzone
111 (arrows) and spot-like signals between neighboring spindles (arrowheads) of Feo colocalizing with
112 Klp3A in anaphase and telophase. On one hand, this observation confirms the combined and
113 colocalized activity of Feo and Klp3A, whereby Feo binding to microtubule overlaps recruits
114 Klp3A to the overlap by increasing the binding affinity[35,44]. On the other hand, and more
115 surprisingly, the signal foci indicate the occurrence of antiparallel microtubule overlaps between
116 neighboring non-sister nuclei across actin furrows and membrane invaginations. This observation
117 led us to question the current paradigm that actin pseudo-compartments prevent microtubule
118 crosslinking between neighboring asters or nuclei. We hypothesize from this localization data that
119 the microtubule-based mechanical connection plays a decisive role in nuclear positioning in
120 preblastoderm and early blastoderm stage embryos.

121 ***Partial knockdown of Feo, Klp3A or Klp61F leads to defective nuclear delivery to the embryo***
122 ***cortex***

123 We wanted to understand the functional implication of the three microtubule binding proteins
124 localizing between non-sister nuclei, and if the function is related to correct nuclear delivery to the
125 embryo cortex. To this end, we perturbed the protein levels of Feo, Klp3A or Klp61F using an
126 RNA interference approach and UAS–Gal4 expression in the germline[52]. We expressed RNAi
127 against these genes individually in the developing *Drosophila* oocyte (Suppl. Fig. 1), while
128 expressing Jupiter::GFP, a microtubule reporter[53], and H2Av::RFP, a chromatin reporter[54]. We

129 exploited the expression kinetics of V32–Gal4 to drive the UASp–RNAi constructs with peak in
130 late oogenesis to prevent undesirable defects during stem cell differentiation. Fertilization in
131 embryos depleted of Feo, Klp3A or Klp61F was similar to the control embryos (data not shown).
132 However, we were unable to determine the exact cycle number when nuclei arrived at the cortex
133 in knockdown embryos. Of note, the interval of division cycles occurring at the cortex and in the
134 cytoplasmic explants remained unaltered when compared to controls. Under all knockdown
135 conditions, we observed nuclei arriving later on average; ~45 min in knockdown condition versus
136 ~15 min in controls, following a 45 min egg laying period. In knockdown embryos, nuclei were
137 irregularly distributed at the cortex and sometimes missing entirely at the posterior end, in contrast
138 to the regular distribution seen in the control RNAi embryo (Fig. 2a, Suppl. Fig. 2). The nuclear
139 density is reduced in the knockdowns as compared to the control (Fig. 2b) but exhibits considerable
140 variability between embryos, which we attributed to the incomplete RNAi. Our analysis revealed
141 embryos with larger areas lacking nuclei (Suppl. Fig. 3a), with anatomically eccentric (Suppl. Fig.
142 3b) and asymmetric nuclear distribution (Suppl. Fig. 3c). Overall, RNAi against Feo resulted in
143 larger distribution changes than RNAi against Klp61F despite similar average internuclear distance
144 (Fig. 2b,c, Suppl. Fig. 3). The internuclear distance distribution is shifted towards longer distances
145 and is more right-tailed for knockdown conditions, while RNAi against Klp3A gave on average
146 the strongest phenotype (Fig. 2c, Suppl. Fig. 3d). We also observed a considerable reduction of
147 fluorescence intensity of Klp3A::GFP at the midzone in Feo knockdown embryos (Suppl. Fig. 4).
148 This confirms Klp3A being downstream of Feo binding to microtubule overlaps[35] and indicates
149 that a reduction of Feo protein concentration by half has a disproportionately stronger effect on
150 Klp3A localization at microtubule overlaps. The irregularity in nuclear position at the cortex
151 increased as the nuclear cycles progressed (Suppl. Video 4). We, sometimes, observed fusion of
152 sister nuclei after mitosis. More interestingly, we also recorded non-sister nuclear movement
153 towards each other in Feo knockdown embryos, leading to fusion of the spindles and over-
154 condensed chromatin. Conversely, fusion was never seen in controls. In summary, the activity of
155 all three microtubule associated proteins is required in the preblastoderm embryo for correct
156 delivery of nuclei to the embryo cortex. However, Kinesin-5 is required for spindle assembly[49,55]
157 and, thus, the phenotype could emerge due to assembly defects rather than post-mitotic nuclear
158 separation. Because depletion of Kinesin-5 led to a mild phenotype despite high knockdown
159 efficiency (Suppl. Fig. 3a), and because of the functional relationship between Feo and Klp3A, we
160 followed up on the role of the latter two genes in internuclear distance maintenance.

161

162 ***Developmental reset ex vivo reveals failure in nuclear distribution upon RNAi knockdown***

163 Our analysis of nuclear distribution during partial knockdown in the embryo suggests that Feo and
164 Klp3A are involved in nuclear delivery to the cortex. However, our protein knockdown approach
165 *in vivo* has two drawbacks that could potentially lead to misinterpretation: (i) the three proteins
166 play a role in spindle midzone function, and their depletion may affect chromosome segregation in
167 anaphase; (ii) The RNAi expression occurs chronically during late oogenesis. Thus, the irregular
168 distribution of nuclei during cortical migration could be due to early sister chromatid separation
169 errors, leading to missing nuclei in the embryo center and exponentially fewer in subsequent
170 division cycles. Alternatively, inefficient nuclear separation following fertilization could lead to
171 spindle fusion and mitotic errors. To circumvent the inability to detect accumulated effects, we
172 performed time-lapse imaging of nuclear division cycles in cytoplasmic explants from
173 preblastoderm embryos that were depleted of either Feo or Klp3A. Because these explants
174 contained only few dividing nuclei, we could follow their distribution, or the failure thereof, while
175 mimicking the very beginning of preblastoderm embryo development. We followed individual
176 nuclei undergoing division cycles and registered the distribution and any fusion events between
177 sister and non-sister nuclei (Fig. 3a). In explants from control embryos, nuclei divide and distribute
178 regularly in the entire explant (Fig. 3a, left, white dashed circle) until a saturated nuclear
179 distribution is reached and mitotic failures in the subsequent cycle are common. The nuclear
180 density at saturation is comparable to nuclear cycle 10 in the intact embryo (1800–2000
181 nuclei/mm^2)[14], corresponding to an internuclear distance of ~25 µm (hexagonal approximation).
182 Strikingly, the nuclei from Feo and Klp3A knockdown embryos also divide consecutively. The
183 average distance between sister nuclei and between non-sister nuclei was lower in the test RNAi
184 as compared to the control (Fig. 3b,c). However, the nuclear position after mitotic separation was
185 maintained in the Feo RNAi while knockdown of Klp3A led to frequent spindle fusion at a
186 comparable nuclear density and accumulation of mitotic failure. Interestingly, spindle length
187 decreased upon depletion of Feo (Fig. 3a), but we did not observe significant decrease in spindle
188 length upon Klp3A depletion as reported earlier, most likely due to inefficient knockdown as
189 compared to deletion[56]. In summary, the reduction of Feo protein expression leads to reduced
190 nuclear separation between sister nuclei and incomplete occupation of nuclei within the explant.
191 However, while a reduction of Feo sustains mitotic divisions, Klp3A knockdown produces a
192 spindle fusion phenotype. It is possible that the absence of Klp3A causes microtubule overlap over-
193 growth and, despite crosslinking by Feo and other MAPs, these long overlaps are not mechanically
194 stiff.

195 ***Displacement of nuclei is rescued in control but not in Feo RNAi embryo explants***

196 To test the model of an astral microtubule crosslinker-based separation mechanism for non-sister
197 nuclei, we took advantage of the amenability of embryo explants for mechanical manipulation and
198 designed an acute perturbation approach. We asked how Feo relocalizes when the distance between
199 two interphase nuclei is manually reduced. Finally, we asked whether, under a Feo knockdown
200 condition, nuclei could still adjust their position when brought in close proximity prior to division.
201 To address these questions, we performed contact micromanipulation and changed the positions of
202 two non-sister nuclei that were just exiting mitosis (Fig. 4a). As the manipulated nuclei continued
203 mitotic progression we registered the localization of Feo::mCherry and measured the nuclear
204 rearrangement during anaphase and telophase of the subsequent cycle. In agreement with our
205 hypothesis, this physical perturbation caused strong localization of Feo::mCherry exclusively in
206 the region between the manipulated nuclei while asters from distant nuclei, which were not
207 manually displaced, did not recruit the microtubule crosslinker detectably (Fig. 4b). Next, we
208 quantified nuclear separation of two neighboring nuclei dividing into four daughter nuclei by
209 determining the four final positions (Fig. 4c), arranging these positions as a quadrilateral, aligning,
210 annotating and overlaying them in a common coordinate system (Fig. 4d,e) and calculating area
211 (Fig. 4f) and lateral distances (Fig. 4g,h). We performed these measurements under the control
212 RNAi condition for nuclei in a large empty cytoplasmic space, in a saturated space where several
213 nuclei have spread through the entire explant (see previous section), and in a crowded explant
214 representing one more division cycle. We found that the area of nuclear separation after
215 manipulation is lower than in the non-manipulated and saturated space but indifferent from the
216 crowded control (Fig. 4f). The manipulated nuclei divided and separated their daughter nuclei at
217 ~15 µm while the distance between non-siblings was maintained at ~25 µm, phenocopying the
218 minimal separation seen in crowded explants (Fig. 4g,h)[28]. Interestingly, these separation distances
219 are similar to what was reported for the blastoderm embryo[57]. Finally, we performed the
220 manipulation of nuclear position in Feo-depleted explants expressing Jupiter::GFP and
221 H2Av::RFP. In these experiments, after manipulation, the daughter nuclei moved towards each
222 other rather than apart (Suppl. Fig. 4c). The separation of siblings was approximately the nuclear
223 diameter (~7 µm) (Fig. 4g, dashed line) and the separation of non-siblings was ~10 µm (Fig. 4h).
224 We conclude that acute repositioning of nuclei is detected by the separation machinery, as reported
225 by Feo, and counteracted to prevent spindle fusion or aggregation of nuclei. In other words, Feo is
226 required to prevent nuclear collisions.

227

228 ***Nuclear separation in the syncytium requires astral microtubule crosslinking by Feo***

229 Feo is a dimer and, *in vitro*, has high affinity for binding two antiparallel microtubules[35,36,44]. In
230 this function, Feo could be generating a repulsive mechanical link – an apparent stiffness – which
231 prevents concentric movement and eventual contact of neighboring nuclei. This model predicts a
232 lower repulsion stiffness in the presence of a monomeric construct of Feo, which binds to the same
233 microtubule lattice binding site as the full-length dimer but does not crosslink the antiparallel
234 microtubules. We expect that this dominant-negative effect can be measured as shorter internuclear
235 distance, irregular separation or frequent nuclear contacts. Thus, we designed two protein
236 expression constructs; one containing the full *feo* coding sequence (sFeoFL::GFP-His_6), the other
237 lacking the N-terminal dimerization domain (sFeoDN::GFP-His_6), both fused with a C-terminal
238 GFP and a His_6 tag sequence (Fig. 5a,c). Proteins were expressed in *E.coli*, affinity-purified and
239 dialyzed into embryo extract compatible buffer[58] (Suppl. Fig. 5a). When these protein constructs
240 were injected into preblastoderm embryos, the first nuclei to arrive at the embryo cortex showed
241 strong GFP signals between dividing chromosomes where the central spindle is located (Fig. 5b,d,
242 arrow). Both constructs were under cell cycle control as the fluorescence disappeared in interphase
243 and reappeared during the next mitosis (Suppl. Video 5). Injection of full-length Feo maintained
244 regular nuclear delivery to the embryo cortex while injection of dominant-negative Feo caused
245 unnatural spindle contacts (Fig. 5d, arrowheads). As in transgenic embryos (Fig. 1f, arrowheads),
246 we also detected small foci of green fluorescence between neighboring nuclei (Fig. 5b, arrowhead),
247 suggesting that the purified protein and the transgenic construct localize identically. Furthermore,
248 when the full-length protein was injected into Feo RNAi embryos the defective nuclear distribution
249 was rescued to a large extent (Suppl. Fig. 5b). Nuclei arrive at the embryo cortex more
250 symmetrically between anterior and posterior ends (Fig. 5e), in a less skewed distribution (Fig. 5f)
251 and with more uniform internuclear distance (Fig. 5g) as compared to mock-injected Feo RNAi
252 embryos. Owing to the variability of injection we could fully recover nuclear density to a normal
253 level in two embryos and significantly increase nuclear density in the remaining five embryos (Fig.
254 5h). Notably, the injected protein pool is stable for at least 90 minutes, throughout several division
255 cycles. In summary, we show that a GFP-tagged full-length protein construct localizes correctly
256 and rescues the gene knockdown in the germline. We conclude that it is functionally identical to
257 the endogenous protein that is maternally deposited in the egg and stable during syncytial
258 development.

259 Finally, having designed and purified the dominant-negative and the full-length protein with
260 identical procedures, we asked how nuclear separation changes upon excess of dominant-negative

261 Feo protein, added at 100–200 nM final concentration to wildtype embryo explants containing one
262 or two nuclei. As control condition, we injected the full-length protein at the same final
263 concentration into embryo explants, and despite this perturbation the explant supported normal
264 nuclear separation and distribution (Fig. 5i, left). Conversely, adding the monomeric
265 sFeoDN::GFP-His_6 construct worsened nuclear separation considerably after chromosomes
266 segregated. Here, in contrast to the control condition, nuclei did not occupy the entire explant space
267 after consecutive divisions (Fig. 5i, right). The short internuclear distance led to unnatural
268 chromosome aggregation, fusion and eventually to mitotic failure. Nuclear separation of two
269 neighboring non-sister nuclei, as measured by the quadrilateral area defined by their position, was
270 significantly smaller than in control divisions in the presence of full-length Feo protein (Fig. 5j,k).
271 We conclude that microtubule crosslinking by Feo, in the presence of Klp3A, generates a repulsive
272 mechanical link between microtubule asters. Thus, it lies at the heart of nuclear separation
273 maintenance during the multinucleated 1-cell stage of *Drosophila* embryo development.

274 Discussion

275 A cornerstone of embryonic development is the formation of a polarized epithelium. Plants and
276 many invertebrates achieve this developmental stage with a unicellular embryo undergoing nuclear
277 proliferation followed by cellularization, a specialized form of cytokinesis[16,59]. Recently, the
278 molecular building blocks and morphogenetic characteristics of cellularization have also been
279 identified as part of the life cycle of a non-animal eukaryote[60]. The offspring of *Sphaeroforma*
280 *arctica* arises from nuclear proliferation, compartmentalization, and plasma membrane
281 invagination generating a proto-epithelium from which newborn cells detach. These observations
282 support the hypothesis that epithelia evolutionary predate animals[61]. We propose that correct
283 compartmentalization and generation of uninuclear offspring necessitates robust nuclear
284 separation. If warranted true, then a separation mechanism must have coevolved with the origin of
285 epithelia and was essential for the emergence of multicellularity.

286 Nuclear proliferation in a coenocyte poses a new challenge: How does the cell safeguard the
287 separation and prevent contact of nuclei while their number increases? Two solutions seem
288 plausible. On one hand, the cell may control the division axes and separate daughter nuclei along
289 linear paths which do not cross. On the other hand, the cell may constrain internuclear distance
290 independent of separation trajectories. Consider two nuclei that are about to divide and separate
291 their progeny along the spindle axis (Fig. 6a). In a 3-dimensional space, none of the daughter nuclei
292 may collide unless the spindle axes are both coplanar and non-parallel. Typically, nuclei migrate
293 only 10–15µm away from the original spindle center before dividing again[28]. This geometric

294 constraint reduces configurations that produce colliding trajectories in a 2-dimensional topology to
295 about 40% of all possible spindle axis orientations, so that axes intersect at an angle between zero
296 (collinear) and 70º (Fig. 6b). Adding complexity, spindles in a network with optimal packing face
297 a number of neighbors (6 in 2D, 12 in 3D) (Fig. 6c). Thus, a synchronously dividing spindle
298 network will inevitably produce colliding trajectories of daughter nuclei. It is therefore necessary
299 that, instead of controlling division axes, the cell controls nuclear proximity independently of the
300 relative orientations they divide (Fig. 6d). This enables the syncytial embryo to divide hundreds of
301 nuclei synchronously and distribute them to any unoccupied position. Here, we demonstrate a
302 molecular mechanism that responds to short internuclear distances in the syncytium with a
303 microtubule dependent repulsion. Each nucleus is associated with a radial array of microtubules
304 nucleated by the centrosome, which duplicates and forms the two spindle poles in the next division.
305 Prior, however, this microtubule aster guides nuclear migration and grows large enough to
306 encounter microtubules from neighboring asters that migrate as well. This encounter leads to
307 interdigitation of the microtubule plus–ends (antiparallel overlaps) and forms binding sites for
308 crosslinking proteins. Our data shows that Feo, the PRC1 homolog in *Drosophila* and antiparallel
309 microtubule crosslinker, plays a central role in defining a minimal internuclear distance in the
310 syncytial *Drosophila* preblastoderm embryo.

311 Vertebrate PRC1 is a microtubule binding protein with high turnover kinetics and at least 28 times
312 higher affinity for antiparallel microtubule overlaps than for single microtubules[35]. This
313 biochemical property, together with fluorescent labeling, renders PRC1 homologs reliable
314 reporters for microtubule aster overlaps in live cell imaging assays[45]. PRC1 crosslinking
315 antiparallel microtubules generates a high affinity binding site for the depolymerase and motor
316 protein Kinesin-4 (Kif4/Xklp1/Klp3A) at the overlap[35,62]. *In vitro*, in addition to maintaining a
317 stable overlap length, co-activity of PRC1 and Xklp1 cause buckling of overlapping microtubules
318 which are immobilized at their minus end[35]. In a sliding assay of taxol-stabilized microtubules, in
319 which microtubules in solution and glass-immobilized microtubules form pairs cross-linked by
320 PRC1, the antiparallel pairs are slid apart by Kif4[63]. This is reminiscent of plus–end directed sliding
321 of Kinesin-5[64] and explains the requirement of PRC1 orthologs for spindle elongation in several
322 species[29,38,39,65]. Indeed, plus–end overlapping microtubules have an apparent mechanical stiffness
323 that is governed by molecular friction and motor activity[63,66]. An assembly of tens of such
324 microtubule pairs generates sufficient mechanical resistance against compressive forces in the
325 nanonewton range, enough to keep two spherical organelles of 5–8 µm diameter and attached to
326 the microtubule minus–ends (MTOC) well separated[67]. Thus, modular upscaling of a single pair

327 into overlapping radial arrays illustrates how the crosslinking mechanism of a Feo and Klp3A
328 decorated antiparallel microtubule pair produces a repulsion between two syncytial nuclei.

329 Feo::GFP expressed in the transgenic line, or supplemented as purified protein, exhibits focal
330 fluorescence signals in the blastoderm embryo and in the explant from preblastoderm embryos.
331 Here we show that the length of these signal foci is surprisingly short and uniform. According to
332 *in vitro* data, and neglecting any regulation other than affinity and depolymerase activity for the
333 underlying microtubule overlap to maintain such a short length, the concentration of Kinesin-4 in
334 the cytoplasm must be at least one magnitude in excess of Feo[35]. Moreover, partial depletion of
335 Feo by RNAi abolishes the signal of Klp3A::GFP below detection, thus considerably reducing the
336 bound fraction of Klp3A at the central spindle. In the embryo, while confirming their already
337 established localization at the spindle midzone[38,43,56,68,69], we recorded Klp3A::GFP signal
338 colocalizing with Feo::mCherry in areas between neighboring spindle asters. However, we could
339 not clearly assess the localization of Klp3A in explants from preblastoderm embryos due to the low
340 signal intensity. A single-copy tagged Klp3A construct expressed with the endogenous promoter
341 failed to provide sufficient signal, and we decided to work with overexpression constructs[70]. This
342 indicates that the microtubule overlap–bound fraction of endogenous Klp3A is comparatively small
343 despite the molar excess in the cytosol as derived from overlap length. Together, these observations
344 point at a protein interaction network localized at antiparallel microtubule overlaps that is sensitive
345 to small changes of Feo. As Feo binds microtubule overlaps independently[35], the phenotypes in
346 intact embryos and in explants could arise due to disproportionate Klp3A perturbation downstream
347 of Feo. In summary, our live-cell microscopy data from blastoderm embryos and preblastoderm
348 embryo explants support the conceptual model proposed by Baker et al.[15] built from individual
349 pairs of microtubules crosslinked and length-regulated by Feo and Klp3A[35]. More importantly, we
350 show how overlapping microtubules in the aster–aster interaction zone[45] form midzone–analogous
351 cytoskeletal assemblies that persist throughout blastoderm development. This is particularly
352 intriguing given that, at the embryo cortex from cycle 10 onwards, actin-based pseudo-furrows
353 form pre-cellular compartments that are thought to prevent nuclear contact[71-74]. In the early
354 blastoderm cycles, however, this compartmentalization may not yet be efficient enough to
355 safeguard nuclear separation, and astral microtubule crosslinking persists as dominant mechanism.
356 This interpretation is further supported by an earlier observation in mutants of the maternal-effect
357 gene *sponge*, embryos of which do not form actin caps and pseudo-furrows in blastoderm stage but
358 depict a homogenous nuclear distribution in cycle 10–11[75].

359 Feo is essential for central spindle assembly and cytokinesis in somatic cells, containing two Cdk
360 phosphorylation sites[34]. Feo, like PRC1 in human cells and Ase1p in fission yeast, is under cell
361 cycle control and undergoes phosphorylation dependent localization from low intensity decoration
362 of metaphase spindle microtubules to a strong localization at the central spindle in anaphase and
363 telophase[29,38,39,44,76]. In the present work, we show that the focal localization of Feo and Klp3A
364 between neighboring nuclei is in synchrony with central spindle localization. It is in this phase of
365 the division cycle when expanding spindles and separating nuclei cause a large spatial perturbation
366 to the positional distribution[57,77]. Thus, a dual role for Feo under cell cycle control emerges; while
367 it targets the central spindle at anaphase onset – forming the spindle midbody – it also binds to
368 astral microtubule overlaps in a phase during which collision prevention is most needed.

369 In *Drosophila* embryos, spindle elongation at anaphase B is mainly powered by the sliding activity
370 of Klp61F[78]. Following the mechanism proposed by Baker et al.[15], and because Klp61F is a
371 candidate crosslinker and slider of overlapping astral microtubules, we performed RNAi
372 knockdown in the germline. Reduction of Klp61F levels to 19% of native levels led to lower density
373 and nonuniform delivery of nuclei to the embryo cortex, confirming its essential role during
374 preblastoderm development. However, owing to the established role of Klp61F in mitosis, the
375 RNAi phenotype could emerge as a consequence of multiple chromosome segregation failures that
376 were undetectable in the preblastoderm embryo. Here, the embryo explant assay overcomes an
377 experimental limitation and enables time-lapse image acquisition of uni- or binuclear explants
378 undergoing multiple divisions. Consequently, we could confirm that Klp61F knockdown led to
379 more frequent division failures rather than shorter nuclear separation. Still, Klp61F and Feo could
380 functionally cooperate in crosslinking astral microtubules because both proteins recognize and bind
381 to microtubule pairs, though with different preference for microtubule orientation[35,36,64,79].
382 Interestingly, a recent study demonstrated that, while Feo modulates binding and localization of
383 Klp61F at the spindle midzone in anaphase, Klp61F cannot functionally rescue the absence of
384 Feo[38]. Presumably, Ase1p/PRC1/Feo binding to microtubule overlaps creates a protein binding hub
385 for motors and regulators[29,35,40,44,68,80]. This property has not been demonstrated for Kinesin-5
386 orthologs. Together, the collection of our and other evidence led us to conclude that Klp61F is not
387 at the core of astral microtubule driven nuclear separation.

388 Lastly, the reader may wonder how astral microtubule overlap crosslinking by Feo and Klp3A
389 defines the internuclear distance metric, leading to a distribution of syncytial nuclei with high
390 regularity. In an earlier study, Telley et al.[28] showed that microtubule aster size varies throughout
391 the nuclear division cycle, reaching a maximum of 11 ± 3 μm in telophase. Herein, the aster size

392 represents the length distribution of microtubules which, for dynamic microtubules with non-
393 growing minus–end, is well approximated with an exponential distribution[81]. We assume that two
394 microtubules from neighboring asters grow at least to average length, overlap with their plus–ends
395 and are collinear. If the overlap length is stably ~1 μm, then the total length from centrosome to
396 centrosome is on average 21 ± 4 μm. Considering that a centrosome is ~1 μm large, and that a
397 nucleus in late telophase is 5 ± 1 μm in diameter, the total distance between the centers of
398 neighboring nuclei is 28 ± 4 μm. This estimate is in good agreement with the internuclear distance
399 distribution measured from center to center of each nucleus (Fig. 3c), the minimal non-sibling
400 internuclear distance in extract (Fig. 4h) and earlier reported separation distances of daughter
401 nuclei[28]. Thus, the short antiparallel overlap length of microtubules from neighboring asters and
402 the microtubule length distribution are sufficient to explain the geometry of nuclear distribution in
403 the *Drosophila* syncytial embryo.

404 **Methods**

405 **Fly husbandry:** Rearing of flies for general maintenance was done as previously described[82]. The
406 following fly lines used to make recombinants or trans-heterozygotes were used: Jupiter::GFP
407 (BDSC# 6836), H2Av::RFP (BDSC# 23650), Feo::GFP (BDSC# 59274), Feo::mCherry (BDSC#
408 59277), Klp61F::GFP (BDSC# 35509), Klp3A::GFP (VDRC# 318352), RNAi targeting Feo
409 (BDSC# 35467), RNAi targeting Klp3A (BDSC# 40944), RNAi targeting Klp3A (BDSC# 43230),
410 RNAi targeting Klp61F (BDSC# 35804), RNAi targeting Klp61F (BDSC# 33685), RNAi targeting
411 mCherry (BDSC# 35785), UASp–GFP (BDSC# 35786).

412 **RNAi experiments:** Knockdown experiments were performed using the TRiPGermline fly lines
413 for RNAi in germline cells[83]. The UAS-hairpin against a gene of interest was expressed using V32–
414 Gal4 (gift from M. Bettencourt Dias) at 25ºC. The expression profile of V32–Gal4 in the oocyte
415 was assessed by dissecting ovaries of flies expressing UASp–GFP at 25ºC and comparing GFP
416 expression at different developmental stages with fluorescence microscopy.

417 **Sample preparation and extraction:** Embryos were collected from apple juice agar plates
418 mounted on a fly cage. They were dechorionated in 7% sodium hypochlorite solution, aligned and
419 immobilized on a clean coverslip using adhesive dissolved in heptane and covered with halocarbon
420 oil (Voltalef 10S). Extraction of cytoplasm from individual embryos and generation of explants
421 was performed on a custom-made microscope as previously described[46,58].

422 **Image acquisition:** Transmission light microscopy images were obtained with a 10x 0.25NA
423 objective, and the polarizer and analyzer of the microscope in crossed configuration. Time-lapse

424 confocal fluorescence Z stacks were acquired on a Yokogawa CSU-W1 spinning disk confocal
425 scanner with 488 nm, 561 nm and 640 nm laser lines. Images of whole embryos were acquired
426 with a 40x 1.3NA oil immersion objective. Images of embryo explants were acquired with a 60x
427 1.2NA or a 40x 1.15NA water immersion objective. Images were recorded with an Andor iXon3
428 888 EMCCD 1024x1024 camera with 13 µm square pixel size, and a 2x magnification in front of
429 the camera except for images used in the analysis of Fig. 5e-h and Supp. Fig. 5b, which were taken
430 by a 20x 0.75NA multi-immersion objective with an Andor Zyla sCMOS 2048x2048 camera with
431 6.5 µm square pixel size.

432 **Image processing:** Image processing i.e. making Z-projections, image cropping, image down-
433 sampling, and video generation, was performed in Fiji[84]. Whole embryo images for knockdown
434 experiments were obtained by pairwise stitching using a plugin in Fiji.

435 **Image analysis:** The fluorescence signal of Feo::GFP in explants was analyzed with the line profile
436 tool in Fiji. First, images of dividing nuclei during anaphase or telophase were filtered with a
437 Gaussian kernel ($\sigma = 1.2$). Spot-like signals located between non-sibling nuclei were identified
438 and, where spots were non-circular, a line was drawn along the longer axis. The angle of the line
439 relative to the image coordinate system was recorded, and an intensity profile was generated.
440 Profiles were aligned relative to the position of highest intensity and averaged. For each image, an
441 intensity profile from a location void of microtubule signal was generated to obtain the background
442 and the standard deviation of Feo::GFP intensity. Finally, the size of the spot was determined by
443 calculating the width of the curve where the intensity was higher than two times the standard
444 deviation of the background. The angle of every profile line was transformed relative to the closer
445 of the two axes that connect the centrosome of one nucleus with the centrosome of the two
446 neighboring sister nuclei (Fig. 1c). A probability density plot of all these relative angles was
447 generated in MATLAB®.

448 The nuclear density in whole embryo images was obtained by measuring the area of the visible
449 part of the embryo after manually tracing the border and dividing the number of nuclei by this area.
450 The localization of nuclei in whole embryos was performed manually in Fiji. The precision of
451 localization was 0.25 µm (intra-operator variability). Localization coordinates were imported into
452 MATLAB® and transformed with respect to the coordinate system of the embryo, as defined by
453 the anterior pole as coordinate origin, and the anterior-posterior axis as *x*-axis. The first-order
454 internuclear distances were obtained from the triangulation connectivity list ('delaunay' function),
455 while excluding any edge connections, and by calculating the distance between the remaining
456 connections. The cumulative distribution function of internuclear distances from individual

457 embryos was obtained with the 'ecdf' function in MATLAB®. An average cumulative distribution
458 function from several embryos was generated by pooling all distances. Next, the deviation of the
459 centroid of nuclear positions from the anatomical center of the embryo was obtained using the
460 formula

461 $$[M_x, M_y] = [C_x, 0] - \left[\frac{1}{n}\sum_{i=1}^{n} x_i\,, \frac{1}{n}\sum_{i=1}^{n} y_i\right]$$

462 whereby an estimate for the anatomical center of the embryo, $[C_x, 0]$ with respect to the embryo
463 coordinate system, is given by half the pole-to-pole distance on the *x*-axis and zero on the *y*-axis.
464 The third-order moment of the distribution of nuclear coordinates was calculated with the
465 'skewness' function in MATLAB®, providing a measure for left-right asymmetry.

466 The measurement of inter-nuclear distances in embryo explants was performed manually in Fiji.
467 The precision of distance measurement was ±0.12 µm as determined by repeated measurement
468 (intra-operator variability). The intensity profile plots of Klp3A::GFP in the Feo RNAi background
469 were obtained using the line profile tool in Fiji, by drawing a line between daughter nuclei in the
470 red (H2Av::RFP) channel and generating an intensity profile plot in the green channel, aligning
471 these profiles according to the peak intensity and averaging profiles from different locations and
472 embryos.

473 Plots of aligned quadrilaterals were generated with MATLAB® by coordinate transformation. The
474 area was calculated using the Gauss trapezoidal formula for general polygons:

475 $$A = \frac{1}{2}\left|\sum_{i=1}^{n-1} x_i y_{i+1} + x_n y_1 - \sum_{i=1}^{n-1} x_{i+1} y_i + x_1 y_n\right|$$

476 While $n = 4$ for 'quadrilaterals'. For each quadrilateral, representing two sets of dividing nuclei,
477 the average of the two involved mitotic separation distances and the average of the two involved
478 non-sibling separations were calculated and plotted. All graphs were made with MATLAB®.

479 **Statistical Analysis:** A Wilcoxon rank-sum test was performed with MATLAB® starting with a
480 significance level $\alpha = 0.05$.

481 **Quantitative PCR:** To measure the transcript levels of *feo*, *klp3A* and *klp61F*, total RNA was
482 extracted following standard procedures (PureLink RNA Mini Kit, Ambion) from embryos
483 collected after 40 minutes of egg laying. A cDNA library was made from Oligo(dT)12–18 as
484 described in the manufacturer's protocol (Transcriptor First Strand cDNA Synthesis Kit, Roche).
485 Quantitative PCR was performed using Quantifast SYBR Green PCR Kit (204052) and QuantiTect

486 Primers for *feo* (QT00919758) in Feo RNAi (35467), *klp3A* (QT00497154) in Klp3A RNAi
487 (40944) and Klp3A RNAi (43230) and *klp61F* (QT00955822) in Klp61F RNAi (35804) and
488 Klp61F RNAi (35685). Actin (QT00498883) was used as a house-keeping gene control.

489 **Cloning, overexpression and purification of sFeoFL::GFP-His$_6$ and sFeoDN::GFP-His$_6$:** The
490 full coding sequence of the *feo* gene fused to a C-terminal GFP tag, was synthesized and codon
491 optimized by NZYTech, referred to herein as sFeoFL::GFP. The DNA was cloned into the vector
492 pET-21a containing a C-terminal His$_6$-tag, and transformed into *E.coli Rosetta* cells. The coding
493 sequence of the *feo* gene without the initial 73 N-terminal residues, referred here as truncated or
494 monomeric sFeoDN::GFP construct, was amplified from the synthesized sFeoFL::GFP construct
495 and re-cloned into the pET-21a vector. Both proteins were produced by IPTG induction at 25ºC.
496 After 4h of incubation, the cells were harvested and resuspended in lysis buffer (100mM K-HEPES
497 pH 7.4, 500 mM NaCl, 10% glycerol, 0.1% Triton X-100, 3 M urea, supplemented with protease
498 inhibitors (Roche) and 100U of DNAse type I (NZYTech)). The cells were lysed using the digital
499 sonifier® (SLPe, Branson) at 70% amplitude with 6 pulses of [30 sec on]-[30 sec off] and clarified
500 by centrifugation at 30'000g for 45 minutes at 4ºC. For purification of the truncated construct, the
501 supernatant was loaded onto a 5 ml HiTrap Chelating HP (GE Healthcare) charged with 0.1 mM
502 $NiCl_2$ and equilibrated with wash buffer (100 mM K-HEPES pH7.4, 500 mM NaCl, 10% glycerol,
503 40 mM imidazole, 1 mM 2-mercaptoethanol), extensively washed with this buffer and eluted with
504 elution buffer (100 mM K-HEPES pH7.4, 500 mM NaCl, 10% glycerol, 500 mM imidazole, 1 mM
505 2-mercaptoethanol) throughout a gradient of 6 CV. For purification of the full-length construct, the
506 supernatant was loaded onto a 1 ml HiTrap TALON crude (GE Healthcare) charged with 50 mM
507 $CoCl_2$ and equilibrated with wash buffer (100 mM K-HEPES pH 7.2, 500 mM NaCl, 10% glycerol,
508 5 mM imidazole, 1 mM 2-mercaptoethanol), extensively washed with this buffer and eluted with
509 elution buffer (100 mM K-HEPES pH 7.2, 500 mM NaCl, 10% glycerol, 150 mM imidazole, 1
510 mM 2-mercaptoethanol), throughout a gradient of 20 CV. Fractions containing the protein of
511 interest were pooled, the buffer exchanged into embryo explant compatible buffer (100 mM K-
512 HEPES pH 7.8, 1 mM $MgCl_2$, 100 mM KCl) using a PD-10 desalting column (GE Healthcare) and
513 concentrated using a 50K MWCO Amicon® Ultracentrifugal filter (Merck). The purifications were
514 performed using the ÄKTApurifier protein purification system (GE Healthcare) and the
515 chromatographic profile of both proteins was followed by measuring the absorbance at 280 nm,
516 254 nm and 488 nm in the UV-900 monitor. The size exclusion method resulted in Feo constructs
517 strongly associated to an unknown contaminant at ~50 kDa. The concentration of each construct
518 was estimated ~50% of the total measured protein concentration based on band analysis of SDS-

519 PAGE. Total protein concentrations were measured with a NanoDrop2000 UV-Vis
520 spectrophotometer (ThermoFisher).

521 **Addition of exogenous proteins:** Purified porcine Tubulin (Cytoskeleton) was labeled with Alexa-
522 647 (Invitrogen, ThermoFisher) following a published protocol[85] and injected into embryos or
523 explants at 0.3–0.8 mg/ml. Purified sFeoFL::GFP and sFeoDN::GFP were injected at 2 mg/ml in
524 EC buffer in embryos or explants. For embryos, the injected volume assumed a spherical shape
525 with diameter D ≈ 0.018 mm, resulting an injection volume of 3.05 x 10^{-6} mm^3. The average length
526 and width of the embryo are 0.5 mm and 0.2 mm, respectively[86]. Assuming an ellipsoid geometry
527 for the embryo, its volume is ~10^{-2} mm^3. Thus, the final concentration of injected protein after
528 equilibration in the entire embryo was 5–6 nM. For explants, both protein constructs were added
529 to explant cytoplasm at 1:200 (vol/vol), resulting in a final concentration in the cytoplasm of 100–
530 200 nM. Importantly, such an excess of full-length Feo protein preserved nuclear divisions and
531 distribution.

532 References

533 1. Gundersen, G. G. & Worman, H. J. Nuclear positioning. *Cell* **152,** 1376–1389 (2013).
534 2. Bone, C. R. & Starr, D. A. Nuclear migration events throughout development. *J. Cell Sci.*
535 **129,** 1951–1961 (2016).
536 3. Minc, N., Burgess, D. & Chang, F. Influence of cell geometry on division-plane positioning.
537 *Cell* **144,** 414–426 (2011).
538 4. Almonacid, M. *et al.* Active diffusion positions the nucleus in mouse oocytes. *Nat. Cell Biol.*
539 **17,** 470–479 (2015).
540 5. Levy, J. R. & Holzbaur, E. L. F. Dynein drives nuclear rotation during forward progression
541 of motile fibroblasts. *J. Cell Sci.* **121,** 3187–3195 (2008).
542 6. Starr, D. A. & Han, M. Role of ANC-1 in tethering nuclei to the actin cytoskeleton. *Science*
543 **298,** 406–409 (2002).
544 7. Almonacid, M. *et al.* Active Fluctuations of the Nuclear Envelope Shape the Transcriptional
545 Dynamics in Oocytes. *Dev. Cell* **51,** 145–157.e10 (2019).
546 8. Neelam, S. *et al.* Direct force probe reveals the mechanics of nuclear homeostasis in the
547 mammalian cell. *Proc. Natl. Acad. Sci. U.S.A.* **112,** 5720–5725 (2015).
548 9. Starr, D. A. & Fridolfsson, H. N. Interactions between nuclei and the cytoskeleton are
549 mediated by SUN-KASH nuclear-envelope bridges. *Annu. Rev. Cell Dev. Biol.* **26,** 421–444
550 (2010).

551 10. Pecreaux, J. *et al.* The Mitotic Spindle in the One-Cell C. elegans Embryo Is Positioned with
552 High Precision and Stability. *Biophys. J.* **111,** 1773–1784 (2016).
553 11. Dassow, von, G. *et al.* Action at a distance during cytokinesis. *J. Cell Biol.* **187,** 831–845
554 (2009).
555 12. Wühr, M., Dumont, S., Groen, A. C., Needleman, D. J. & Mitchison, T. J. How does a
556 millimeter-sized cell find its center? *Cell Cycle* **8,** 1115–1121 (2009).
557 13. Gibeaux, R., Politi, A. Z., Philippsen, P. & Nedelec, F. Mechanism of nuclear movements in
558 a multinucleated cell. *Mol. Biol. Cell* **28,** 645–660 (2017).
559 14. Foe, V. E. & Alberts, B. M. Studies of nuclear and cytoplasmic behaviour during the five
560 mitotic cycles that precede gastrulation in Drosophila embryogenesis. *J. Cell Sci.* **61,** 31–70
561 (1983).
562 15. Baker, J., Theurkauf, W. E., Theurkauf, W. E. & Schubiger, G. Dynamic changes in
563 microtubule configuration correlate with nuclear migration in the preblastoderm Drosophila
564 embryo. *J. Cell Biol.* **122,** 113–121 (1993).
565 16. Lecuit, T. & Wieschaus, E. Polarized insertion of new membrane from a cytoplasmic
566 reservoir during cleavage of the Drosophila embryo. *J. Cell Biol.* **150,** 849–860 (2000).
567 17. Callaini, G., Dallai, R. & Riparbelli, M. G. Cytochalasin induces spindle fusion in the
568 syncytial blastoderm of the early Drosophila embryo. *Biol. Cell* **74,** 249–254 (1992).
569 18. Kankel, M. W., Duncan, D. M. & Duncan, I. A screen for genes that interact with the
570 Drosophila pair-rule segmentation gene fushi tarazu. *Genetics* **168,** 161–180 (2004).
571 19. Bhat, K. M. *et al.* The GAGA factor is required in the early Drosophila embryo not only for
572 transcriptional regulation but also for nuclear division. *Development* **122,** 1113–1124 (1996).
573 20. Kao, L.-R. & Megraw, T. L. Centrocortin cooperates with centrosomin to organize
574 Drosophila embryonic cleavage furrows. *Curr. Biol.* **19,** 937–942 (2009).
575 21. Megraw, T. L., Li, K., Kao, L. R. & Kaufman, T. C. The centrosomin protein is required for
576 centrosome assembly and function during cleavage in Drosophila. *Development* **126,** 2829–
577 2839 (1999).
578 22. Vaizel-Ohayon, D. & Schejter, E. D. Mutations in centrosomin reveal requirements for
579 centrosomal function during early Drosophila embryogenesis. *Curr. Biol.* **9,** 889–898 (1999).
580 23. Dassow, von, G. & Schubiger, G. How an actin network might cause fountain streaming and
581 nuclear migration in the syncytial Drosophila embryo. *J. Cell Biol.* **127,** 1637–1653 (1994).
582 24. Hatanaka, K. & Okada, M. Retarded nuclear migration in Drosophila embryos with aberrant
583 F-actin reorganization caused by maternal mutations and by cytochalasin treatment.
584 *Development* **111,** 909–920 (1991).

585 25. Royou, A., Field, C., Sisson, J. C., Sullivan, W. & Karess, R. Reassessing the role and
586 dynamics of nonmuscle myosin II during furrow formation in early Drosophila embryos.
587 *Mol. Biol. Cell* **15,** 838–850 (2004).
588 26. Wheatley, S., Kulkarni, S. & Karess, R. Drosophila nonmuscle myosin II is required for rapid
589 cytoplasmic transport during oogenesis and for axial nuclear migration in early embryos.
590 *Development* **121,** 1937–1946 (1995).
591 27. Deneke, V. E. *et al.* Self-Organized Nuclear Positioning Synchronizes the Cell Cycle in
592 Drosophila Embryos. *Cell* **177,** 925–941.e17 (2019).
593 28. Telley, I. A., Gáspár, I., Ephrussi, A. & Surrey, T. Aster migration determines the length
594 scale of nuclear separation in the Drosophila syncytial embryo. *J. Cell Biol.* **197,** 887–895
595 (2012).
596 29. Khmelinskii, A., Roostalu, J., Roque, H., Antony, C. & Schiebel, E. Phosphorylation-
597 dependent protein interactions at the spindle midzone mediate cell cycle regulation of spindle
598 elongation. *Dev. Cell* **17,** 244–256 (2009).
599 30. Scholey, J. M., Civelekoglu-Scholey, G. & Brust-Mascher, I. Anaphase B. *Biology (Basel)*
600 **5,** 51 (2016).
601 31. Cheerambathur, D. K., Gassmann, R., Cook, B., Oegema, K. & Desai, A. Crosstalk between
602 microtubule attachment complexes ensures accurate chromosome segregation. *Science* **342,**
603 1239–1242 (2013).
604 32. Reinemann, D. N. *et al.* Collective Force Regulation in Anti-parallel Microtubule Gliding by
605 Dimeric Kif15 Kinesin Motors. *Curr. Biol.* **27,** 2810–2820.e6 (2017).
606 33. Tao, L. *et al.* A homotetrameric kinesin-5, KLP61F, bundles microtubules and antagonizes
607 Ncd in motility assays. *Curr. Biol.* **16,** 2293–2302 (2006).
608 34. Vernì, F. *et al.* Feo, the Drosophila homolog of PRC1, is required for central-spindle
609 formation and cytokinesis. *Curr. Biol.* **14,** 1569–1575 (2004).
610 35. Bieling, P., Telley, I. A. & Surrey, T. A minimal midzone protein module controls formation
611 and length of antiparallel microtubule overlaps. *Cell* **142,** 420–432 (2010).
612 36. Subramanian, R. *et al.* Insights into antiparallel microtubule crosslinking by PRC1, a
613 conserved nonmotor microtubule binding protein. *Cell* **142,** 433–443 (2010).
614 37. Kwon, M. & Scholey, J. M. Spindle mechanics and dynamics during mitosis in Drosophila.
615 *Trends Cell Biol.* **14,** 194–205 (2004).
616 38. Wang, H., Brust-Mascher, I. & Scholey, J. M. The microtubule cross-linker Feo controls the
617 midzone stability, motor composition, and elongation of the anaphase B spindle in
618 Drosophila embryos. *Mol. Biol. Cell* **26,** 1452–1462 (2015).

619 39. Zhu, C., Lau, E., Schwarzenbacher, R., Bossy-Wetzel, E. & Jiang, W. Spatiotemporal control
620 of spindle midzone formation by PRC1 in human cells. *Proc. Natl. Acad. Sci. U.S.A.* **103,**
621 6196–6201 (2006).
622 40. Hu, C.-K., Ozlü, N., Coughlin, M., Steen, J. J. & Mitchison, T. J. Plk1 negatively regulates
623 PRC1 to prevent premature midzone formation before cytokinesis. *Mol. Biol. Cell* **23,** 2702–
624 2711 (2012).
625 41. Williams, B. C., Dernburg, A. F., Puro, J., Nokkala, S. & Goldberg, M. L. The Drosophila
626 kinesin-like protein KLP3A is required for proper behavior of male and female pronuclei at
627 fertilization. *Development* **124,** 2365–2376 (1997).
628 42. Bringmann, H. *et al.* A kinesin-like motor inhibits microtubule dynamic instability. *Science*
629 **303,** 1519–1522 (2004).
630 43. Kwon, M. *et al.* The chromokinesin, KLP3A, dives mitotic spindle pole separation during
631 prometaphase and anaphase and facilitates chromatid motility. *Mol. Biol. Cell* **15,** 219–233
632 (2004).
633 44. Subramanian, R., Ti, S.-C., Tan, L., Darst, S. A. & Kapoor, T. M. Marking and measuring
634 single microtubules by PRC1 and kinesin-4. *Cell* **154,** 377–390 (2013).
635 45. Nguyen, P. A. *et al.* Spatial organization of cytokinesis signaling reconstituted in a cell-free
636 system. *Science* **346,** 244–247 (2014).
637 46. de-Carvalho, J., Deshpande, O., Nabais, C. & Telley, I. A. A cell-free system of Drosophila
638 egg explants supporting native mitotic cycles. *Methods Cell Biol.* **144,** 233–257 (2018).
639 47. Cheerambathur, D. K., Brust-Mascher, I., Civelekoglu-Scholey, G. & Scholey, J. M.
640 Dynamic partitioning of mitotic kinesin-5 cross-linkers between microtubule-bound and
641 freely diffusing states. *J. Cell Biol.* **182,** 429–436 (2008).
642 48. Sharp, D. J., Yu, K. R., Sisson, J. C., Sullivan, W. & Scholey, J. M. Antagonistic microtubule-
643 sliding motors position mitotic centrosomes in Drosophila early embryos. *Nature Cell*
644 *Biology* **1,** 51–54 (1999).
645 49. Heck, M. M. *et al.* The kinesin-like protein KLP61F is essential for mitosis in Drosophila. *J.*
646 *Cell Biol.* **123,** 665–679 (1993).
647 50. Mavrakis, M., Rikhy, R. & Lippincott-Schwartz, J. Plasma membrane polarity and
648 compartmentalization are established before cellularization in the fly embryo. *Dev. Cell* **16,**
649 93–104 (2009).
650 51. Kotadia, S., Crest, J., Tram, U., Riggs, B. & Sullivan, W. *Blastoderm Formation and*
651 *Cellularisation in Drosophila melanogaster*. **122,** 113– (American Cancer Society, 2001),
652 ISBN 0470016175.

653 52. Staller, M. V. *et al.* Depleting gene activities in early Drosophila embryos with the 'maternal-
654 Gal4-shRNA' system. *Genetics* **193,** 51–61 (2013).
655 53. Morin, X., Daneman, R., Zavortink, M. & Chia, W. A protein trap strategy to detect GFP-
656 tagged proteins expressed from their endogenous loci in Drosophila. *Proc. Natl. Acad. Sci.*
657 *U.S.A.* **98,** 15050–15055 (2001).
658 54. Schuh, M., Schuh, M., Lehner, C. F. & Heidmann, S. Incorporation of Drosophila
659 CID/CENP-A and CENP-C into centromeres during early embryonic anaphase. *Curr. Biol.*
660 **17,** 237–243 (2007).
661 55. Sawin, K. E., LeGuellec, K., Philippe, M. & Mitchison, T. J. Mitotic spindle organization by
662 a plus-end-directed microtubule motor. *Nature* **359,** 540–543 (1992).
663 56. Williams, B. C., Riedy, M. F., Williams, E. V., Gatti, M. & Goldberg, M. L. The Drosophila
664 kinesin-like protein KLP3A is a midbody component required for central spindle assembly
665 and initiation of cytokinesis. *J. Cell Biol.* **129,** 709–723 (1995).
666 57. Kanesaki, T., Edwards, C. M., Schwarz, U. S. & Grosshans, J. Dynamic ordering of nuclei
667 in syncytial embryos: a quantitative analysis of the role of cytoskeletal networks. *Integr. Biol.*
668 **3,** 1112–1119 (2011).
669 58. Telley, I. A., Gáspár, I., Ephrussi, A. & Surrey, T. A single Drosophila embryo extract for
670 the study of mitosis ex vivo. *Nat. Protoc.* **8,** 310–324 (2013).
671 59. Hehenberger, E., Kradolfer, D. & Köhler, C. Endosperm cellularization defines an important
672 developmental transition for embryo development. *Development* **139,** 2031–2039 (2012).
673 60. Dudin, O. *et al.* A unicellular relative of animals generates a layer of polarized cells by
674 actomyosin-dependent cellularization. *Elife* **8,** 3123 (2019).
675 61. Dickinson, D. J., Nelson, W. J. & Weis, W. I. An epithelial tissue in Dictyostelium challenges
676 the traditional origin of metazoan multicellularity. *Bioessays* **34,** 833–840 (2012).
677 62. Kurasawa, Y., Earnshaw, W. C., Mochizuki, Y., Dohmae, N. & Todokoro, K. Essential roles
678 of KIF4 and its binding partner PRC1 in organized central spindle midzone formation. *EMBO*
679 *J.* **23,** 3237–3248 (2004).
680 63. Wijeratne, S. & Subramanian, R. Geometry of antiparallel microtubule bundles regulates
681 relative sliding and stalling by PRC1 and Kif4A. *Elife* **7,** 37782 (2018).
682 64. Kapitein, L. C. *et al.* The bipolar mitotic kinesin Eg5 moves on both microtubules that it
683 crosslinks. *Nature* **435,** 114–118 (2005).
684 65. Schuyler, S. C., Liu, J. Y. & Pellman, D. The molecular function of Ase1p: evidence for a
685 MAP-dependent midzone-specific spindle matrix. Microtubule-associated proteins. *J. Cell*
686 *Biol.* **160,** 517–528 (2003).

687 66. Forth, S., Hsia, K.-C., Shimamoto, Y. & Kapoor, T. M. Asymmetric friction of nonmotor
688 MAPs can lead to their directional motion in active microtubule networks. *Cell* **157,** 420–
689 432 (2014).
690 67. Lele, T. P., Dickinson, R. B. & Gundersen, G. G. Mechanical principles of nuclear shaping
691 and positioning. *J. Cell Biol.* **217,** 3330–3342 (2018).
692 68. D'Avino, P. P. *et al.* Recruitment of Polo kinase to the spindle midzone during cytokinesis
693 requires the Feo/Klp3A complex. *PLoS ONE* **2,** e572 (2007).
694 69. Page, S. L. & Hawley, R. S. The Drosophila meiotic mutant mei-352 is an allele of klp3A
695 and reveals a role for a kinesin-like protein in crossover distribution. *Genetics* **170,** 1797–
696 1807 (2005).
697 70. Sarov, M. *et al.* A genome-wide resource for the analysis of protein localisation in
698 Drosophila. *Elife* **5,** e12068 (2016).
699 71. Karr, T. L. & Alberts, B. M. Organization of the cytoskeleton in early Drosophila embryos.
700 *J. Cell Biol.* **102,** 1494–1509 (1986).
701 72. Kellogg, D. R., Mitchison, T. J. & Alberts, B. M. Behaviour of microtubules and actin
702 filaments in living Drosophila embryos. *Development* **103,** 675–686 (1988).
703 73. Mavrakis, M., Rikhy, R. & Lippincott-Schwartz, J. Cells within a cell: Insights into cellular
704 architecture and polarization from the organization of the early fly embryo. *Commun. Integr.*
705 *Biol.* **2,** 313–314 (2009).
706 74. Lecuit, T. Junctions and vesicular trafficking during Drosophila cellularization. *J. Cell Sci.*
707 **117,** 3427–3433 (2004).
708 75. Postner, M. A., Miller, K. G., Wieschaus, E. F. & Wieschaus, E. F. Maternal effect mutations
709 of the sponge locus affect actin cytoskeletal rearrangements in Drosophila melanogaster
710 embryos. *J. Cell Biol.* **119,** 1205–1218 (1992).
711 76. Polak, B., Risteski, P., Lesjak, S. & Tolić, I. M. PRC1-labeled microtubule bundles and
712 kinetochore pairs show one-to-one association in metaphase. *EMBO Rep.* **18,** 217–230
713 (2017).
714 77. Lv, Z. *et al.* The emergent Yo-yo movement of nuclei driven by collective cytoskeletal
715 remodeling in pseudo-synchronous mitotic cycles. *bioRxiv* **22,** 662965 (2019).
716 78. Brust-Mascher, I., Sommi, P., Cheerambathur, D. K. & Scholey, J. M. Kinesin-5-dependent
717 poleward flux and spindle length control in Drosophila embryo mitosis. *Mol. Biol. Cell* **20,**
718 1749–1762 (2009).
719 79. Kellogg, E. H. *et al.* Near-atomic cryo-EM structure of PRC1 bound to the microtubule. *Proc.*
720 *Natl. Acad. Sci. U.S.A.* **113,** 9430–9439 (2016).

721 80. Sasabe, M. & Machida, Y. MAP65: a bridge linking a MAP kinase to microtubule turnover.
722 *Curr. Opin. Plant Biol.* **9,** 563–570 (2006).
723 81. Howard, J. *Mechanics of Motor Proteins and the Cytoskeleton*. Sinauer Associates
724 Incorporated (2001), ISBN 0-87893-334-4.
725 82. Stocker, H. & Gallant, P. Getting started: an overview on raising and handling Drosophila.
726 *Methods Mol. Biol.* **420,** 27–44 (2008).
727 83. Perkins, L. A. *et al.* The Transgenic RNAi Project at Harvard Medical School: Resources
728 and Validation. *Genetics* **201,** 843–852 (2015).
729 84. Schindelin, J. *et al.* Fiji: an open-source platform for biological-image analysis. *Nat. Meth.*
730 **9,** 676–682 (2012).
731 85. Hyman, A. A. Preparation of marked microtubules for the assay of the polarity of
732 microtubule-based motors by fluorescence. *J. Cell Sci. Suppl.* **14,** 125–127 (1991).
733 86. Markow, T. A., Beall, S. & Matzkin, L. M. Egg size, embryonic development time and
734 ovoviviparity in Drosophila species. *J. Evol. Biol.* **22,** 430–434 (2008).
735

736 ## Acknowledgements

737 We thank members of the Telley lab for fruitful discussions, Jonathon Scholey for constructive
738 comments on the manuscript and for fly stocks, and Thomas Surrey for discussions throughout the
739 project. We thank the staff of the Fly Facility, the Advanced Imaging Facility and the Technical
740 Support Service at the Instituto Gulbenkian de Ciência (IGC). Transgenic fly stocks were obtained
741 from the Vienna Drosophila Resource Center and Bloomington Drosophila Stock Center (NIH
742 P40OD018537). We acknowledge financial support provided by Fundação Calouste Gulbenkian
743 (FCG), European Commission FP7 Marie Curie CIG to I.A.T. (PCIG13-GA-2013-618743),
744 Human Frontiers Science Program YIG to I.A.T. (RGY0083/2016), a doctoral fellowship
745 SFRH/BD/52174/2013 to O.D. from Fundação para a Ciência e a Tecnologia (FCT). We
746 acknowledge LISBOA-01-0145-FEDER-007654 supporting IGC's core operation, LISBOA-01-
747 0145-FEDER-022170 (*Congento*) supporting the Fly Facility, and PPBI-POCI-01-0145-FEDER-
748 022122 supporting the Advanced Imaging Facility, all co-financed by FCT (Portugal) and
749 Lisboa2020, under the PORTUGAL2020 agreement (European Regional Development Fund).

750 ## Author contributions

751 OD, JC and IAT conceived and designed the project. OD and IAT designed experiments and OD
752 performed them with support from JC. DMV and OD designed, purified and characterized the
753 protein constructs. OD and IAT prepared the figures and wrote the manuscript.

754

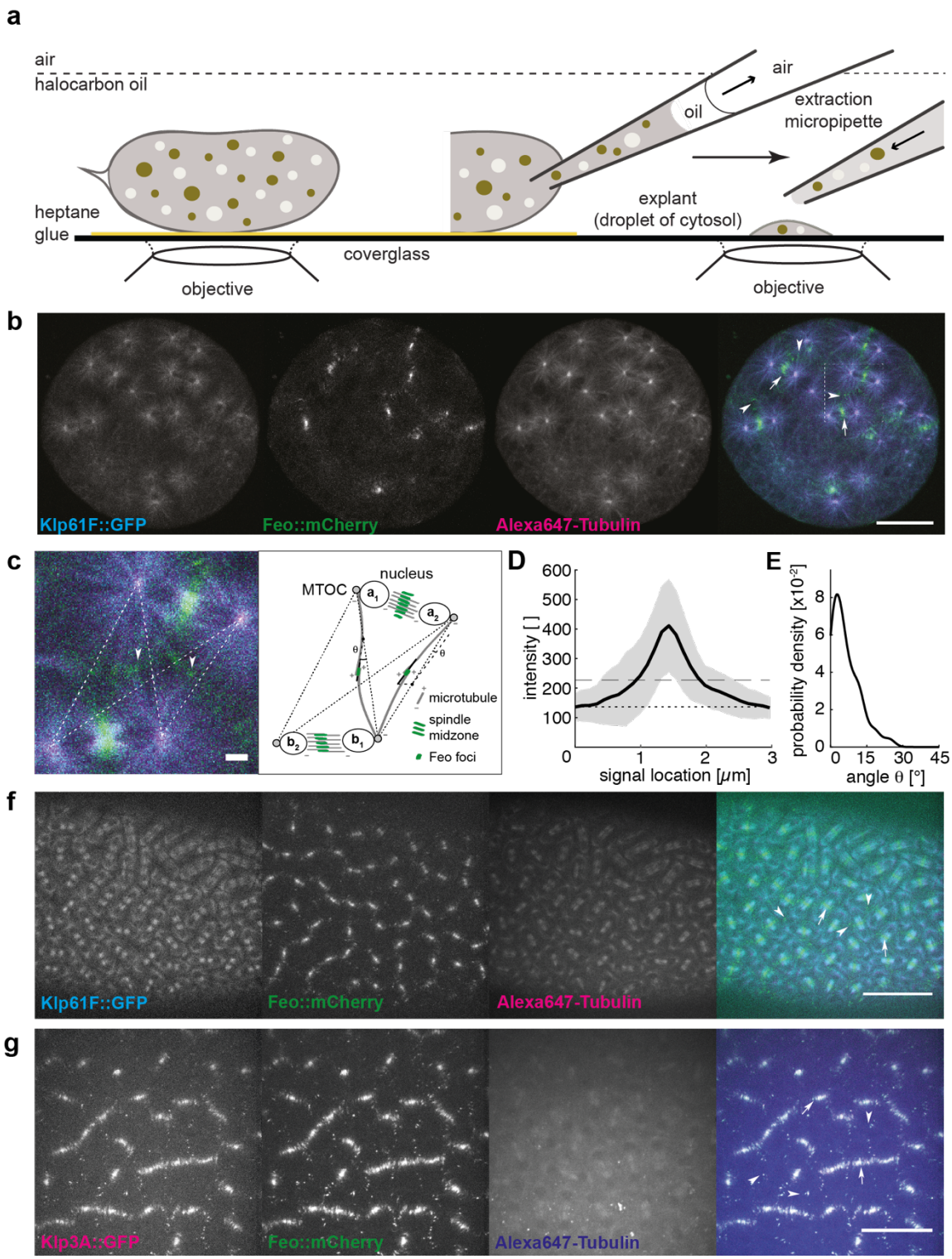

Figure 1: Feo, Klp3A and Klp61F localization confirm antiparallel microtubule overlaps between asters of non-sister nuclei.

a) Schematic showing a *Drosophila* syncytial embryo immobilized to the coverslip and covered with a thin layer of halocarbon oil ready for time-lapse microscopy. On the right, an embryo that is developmentally staged preblastoderm is punctured for extraction and deposition of cytosol on the coverslip using a micropipette, thereby generating a series of embryo explants. **b)** Three-color snapshot from a time-lapse (Suppl. Video 1) of an explant generated from an embryo expressing

Klp61F::GFP (cyan), Feo::mCherry (green) and injected with Alexa647–Tubulin (magenta). The antiparallel microtubule crosslinker, Feo, localizes strongly to the spindle midzone during the anaphase/telophase transition (arrows) and to the intercalating microtubules from neighboring nuclei (arrowheads). Scale bar, 30 µm. **c)** Zoom-in of the merged color channel image in b) (dashed square) demonstrating how Feo localizes as intense foci between neighboring spindles, where microtubules from non-sister nuclei meet (arrowheads). The schematic on the right represents the configuration shown in the image, exemplifying the location of the two pairs of sister nuclei, a^1–a^2 and b^1–b^2, and two representative Feo foci. The dashed lines represent the shortest path of microtubule interactions between the centrosomes (C) of non-sister nuclei. An intensity profile of the foci is generated by drawing a line (continuous) along the longest axis and centered to the foci. The angle θ relative to the dashed interaction line is determined. Scale bar, 2 µm. **d)** The average intensity profile of Feo foci indicate a foci length of 1.0 ± 0.35 µm. The grey area designates the standard deviation (SD), the dotted line marks the background level, and the dashed line marks two times SD above the background. N = 7; n = 57. **e)** The distribution of angles (θ) suggests that the antiparallel microtubule overlaps occur mostly along the connecting line between the neighboring non-sister nuclei. N = 7; n = 42. Cases where foci were symmetric and a long axis could not be determined were excluded from the analysis. **f)** Three-color snapshot of a blastoderm embryo expressing Klp61F::GFP (cyan), Feo::mCherry (green) and injected with Alexa647–Tubulin (magenta) showing that Feo localizes strongly between sister nuclei as part of the spindle midzone (arrows) and, more strikingly, between neighboring non-sister nuclei as distinct foci (arrowheads). Scale bar, 50 µm. Refer to Suppl. Video 2. **g)** Three-color snapshot of a blastoderm embryo expressing Klp3A::GFP (magenta), Feo::mCherry (green) and injected with Alexa647–Tubulin (blue) showing that Klp3A co-localizes with Feo at the spindle midzone (arrows) and at the foci between neighboring non-sister nuclei (arrowheads). Scale bar, 50 µm. Refer to Suppl. Video 3.

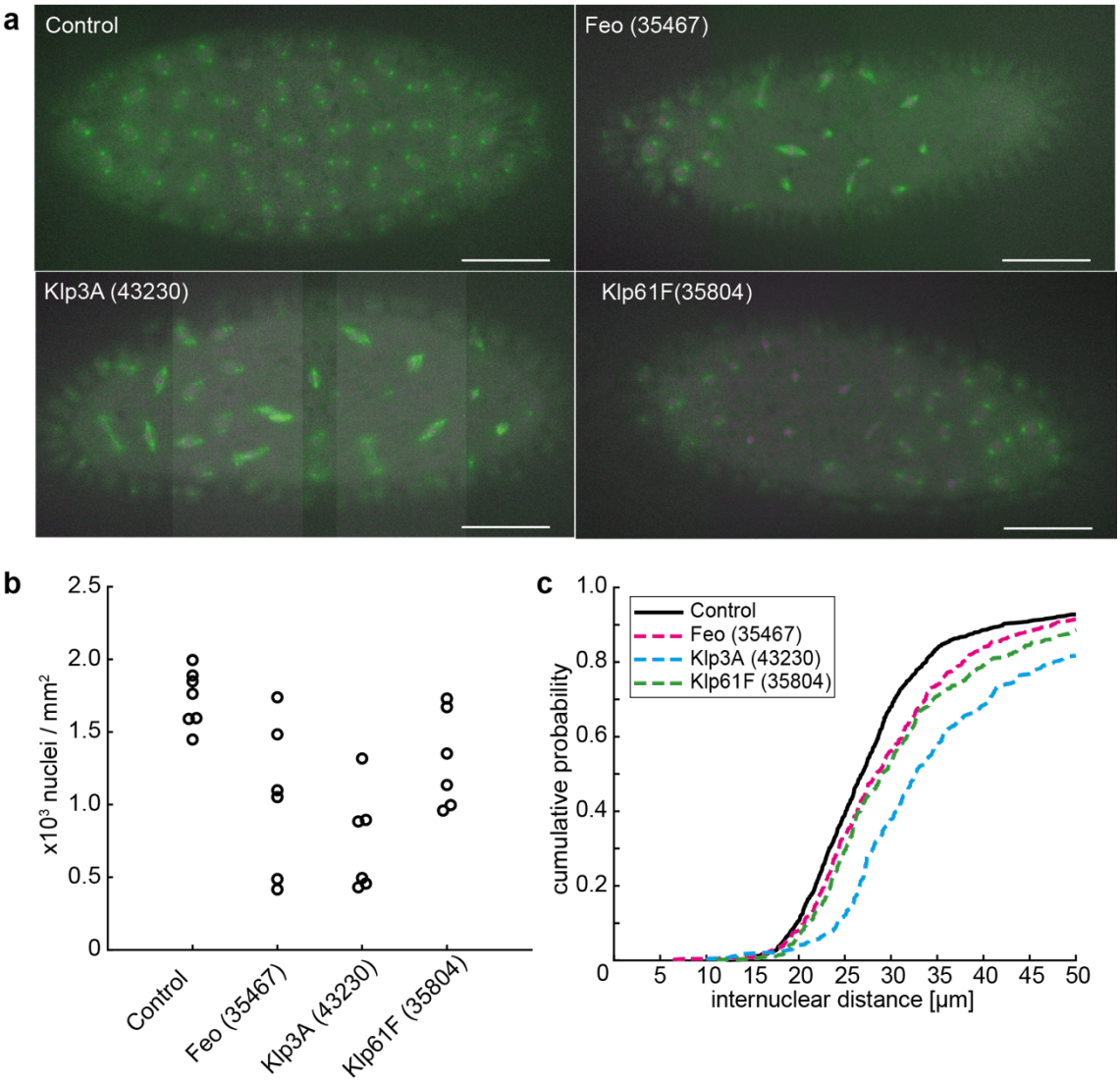

Figure 2: Partial knockdown of Feo, Klp3a or Klp61F by RNAi leads to defective nuclear delivery to the embryo cortex.

a) Maximum intensity projections from three-dimensional time-lapse movies of embryos partially depleted of Feo, Klp3A or Klp61F, expressing Jupiter::GFP (green) marking microtubules and H2Av::RFP (magenta) marking chromatin. Knockdown embryos show irregular nuclear distribution during the first interphase occurring at the cortex as compared to the regular nuclear distribution in control embryos (RNAi against mCherry). Scale bar, 50 µm. **b)** A quantification of the number of nuclei per square millimeter shows a higher degree of variation between the six embryos knocked down for either of the three genes Feo (35467), Klp3A (43230) or Klp61F (35804) as compared to control embryos. In all cases the density is decreased on average. Each data point represents one embryo. **c)** The cumulative probability function of the internuclear distance between first-order neighbors in embryos depleted of Feo, Klp3A or Klp61F shows on average a higher internuclear distance. Thus, the number of nuclei at the cortex is smaller with broader distribution indicating greater irregularity with respect to the control. N = 7 (control), N = 6 (RNAi lines). Refer to Suppl. Fig. 2 and Video 4.

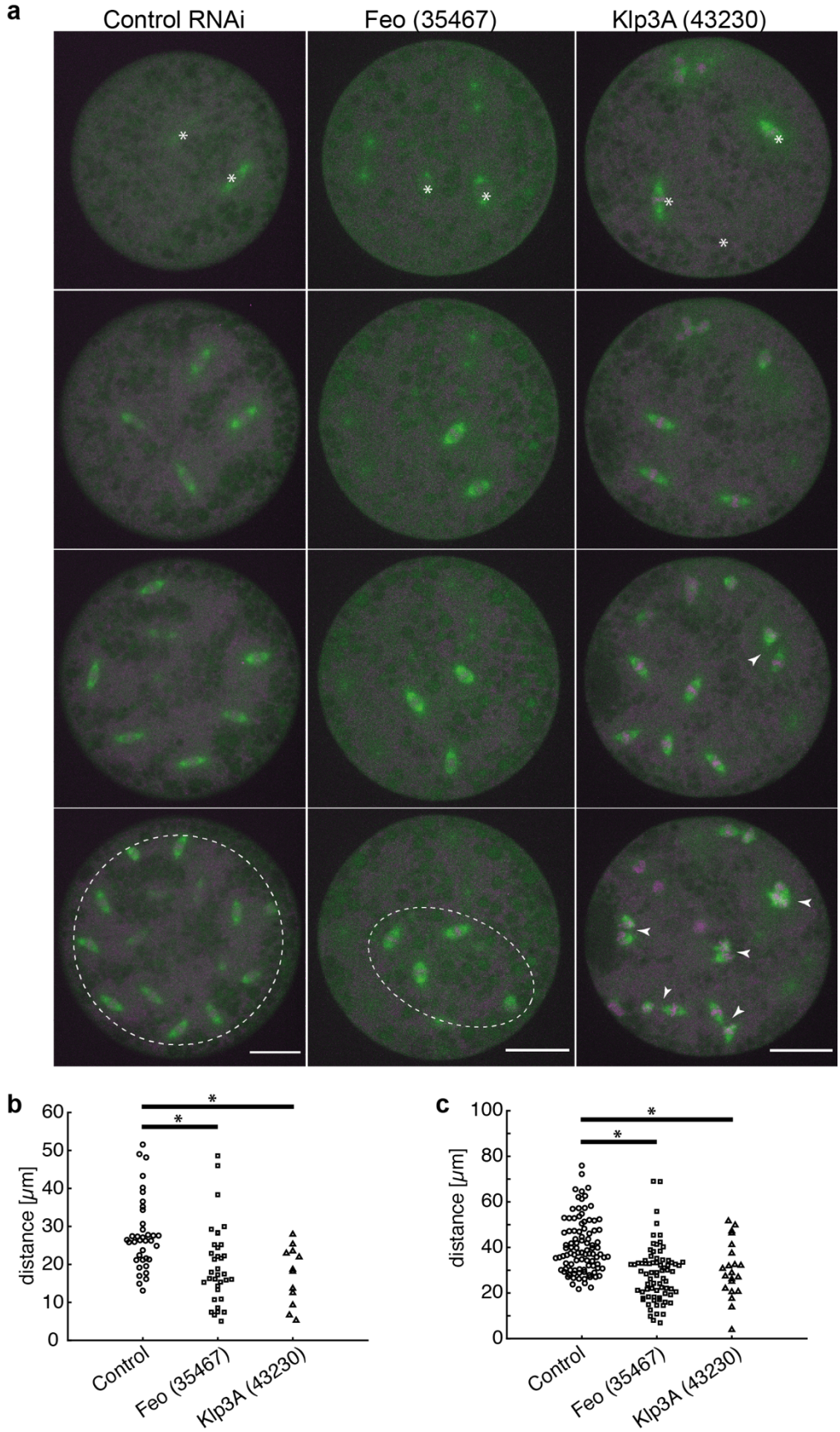

803

804 **Figure 3: Partial knockdown of Feo, Klp3a or Klp61F by RNAi leads to defective nuclear**
805 **distribution in preblastoderm embryo explants.**

a) Maximum intensity projections from time-lapse movies of embryo explants under control conditions and partial depletion of Feo, Klp3A or Klp61F, while expressing Jupiter::GFP (green) marking microtubules and H2Av::RFP (magenta) marking chromatin. Each panel shows metaphase of consecutive division. White stars in the first frame mark the position of dividing nuclei (sometimes out of focus). The control explants (RNAi against mCherry) undergo normal nuclear divisions and distribute the daughter nuclei within the entire explant volume (dashed circle). Explants from Feo depleted embryos undergo mitotic nuclear divisions but daughter nuclei separate less efficiently, leading to a partial occupation of the cytoplasm (dashed ellipse). Explants from Klp3A depleted embryos undergo mitotic nuclear divisions with slightly less efficient distribution than in controls and with higher prevalence for spindle fusion (arrowheads). Scale bar, 30 µm; time in min:sec. **b)** Separation distance between daughter nuclei after mitotic nuclear division under control conditions and under knockdown for Feo (35467) and Klp3A (43230) in embryo explants. Separation distance is significantly reduced in both knock-down conditions (Control: $N = 4$, $n = 38$; Feo (35467): $N = 2$, $n = 36$; Klp3A (43230): $N = 3$, $n = 23$; $p < 0.01$, Wilcoxon signed-rank test). **c)** Separation distance between first-neighbor non-sibling nuclei measured between mitotic divisions under control conditions and under knockdown for Feo (35467) and Klp3A (43230) in embryo explants. The separation distance is significantly shorter in both knock-down conditions (Control: $N = 3$, $n = 98$; Feo (35467): $N = 3$, $n = 77$; Klp3A (43230): $N = 3$, $n = 50$; $p < 0.05$, Wilcoxon signed-rank test) though the effect is stronger when Feo is depleted.

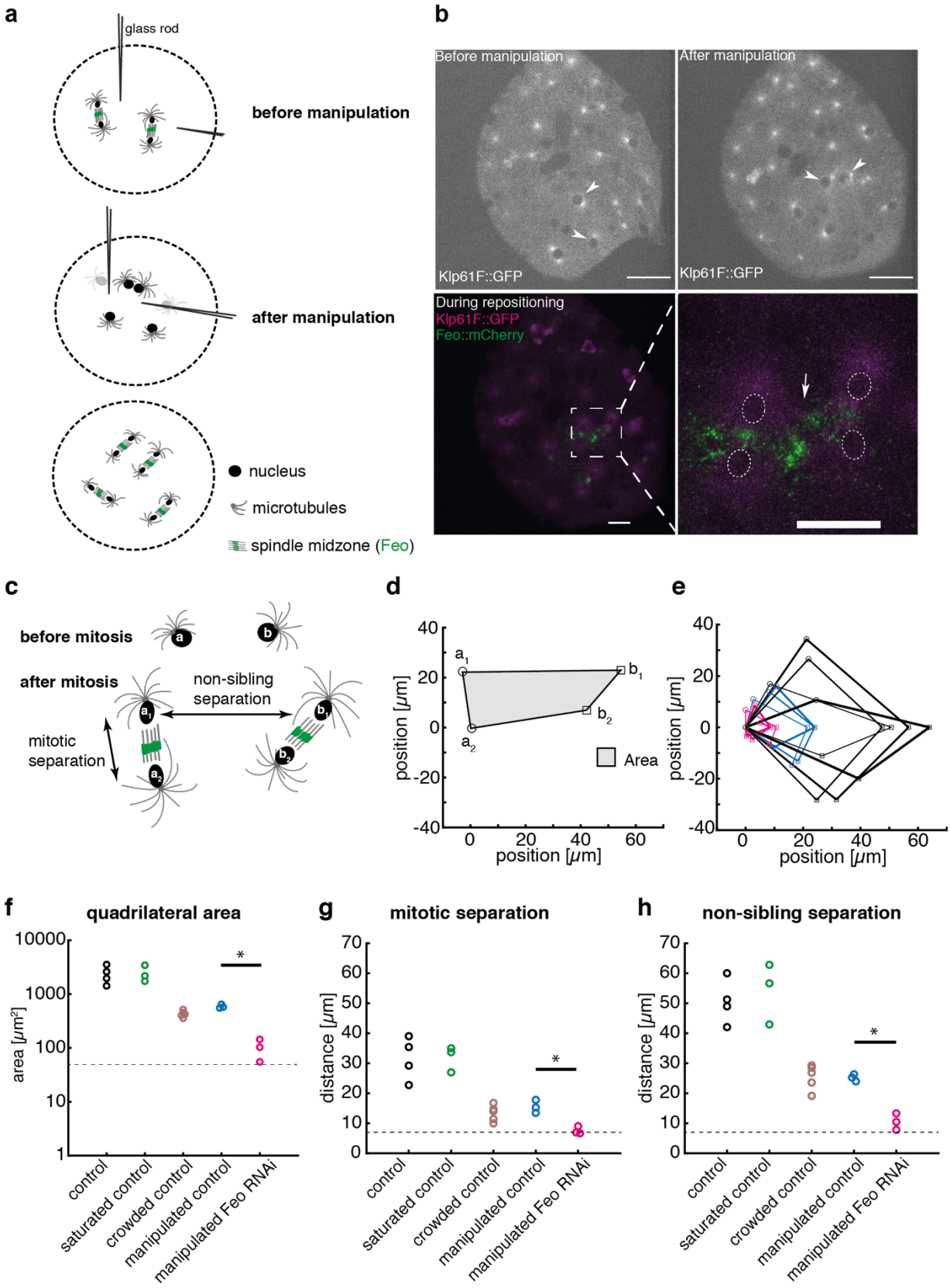

826

827 **Figure 4: Feo depleted explants fail to maintain nuclear separation distance following acute**
828 **physical manipulation.**

a) Scheme showing the manipulation of internuclear distance in embryo explants. After a mitotic division and nuclear separation, two non-sister nuclei are brought close to each other during anaphase B–telophase by means of two glass rods. Subsequently, nuclei divide again, and daughter nuclei are separated at defined distances. **b)** Fluorescence images illustrating physical manipulation of nuclear position in an explant made from an embryo expressing Klp61F::GFP (green) marking microtubules positively and nuclei negatively due to exclusion (dark disks), together with Feo::mCherry (magenta). The top row shows the GFP signal before (left) and after (right) manipulation. Physical manipulation decreased the distance selectively between two nuclei (arrowheads). Scale bar, 30 µm. Upon conclusion of the next mitosis and during repositioning of the daughter nuclei (bottom), Feo localizes exclusively between the daughters of manipulated nuclei (zoom on the right), indicating that microtubule overlaps have formed. In contrast, Feo localization is not detectable between nuclei that have not been moved and are further apart. Scale bars, 15 µm **c)** Schematic of the mitotic separation distance and non-sister separation distance. Nuclei a and b were brought close to each other and following a division give rise to daughters a_1, a_2, and b_1, b_2, respectively. **d)** Schematic of the quadrilateral area defined by the four nuclei a_1, a_2, b_1, b_2 after mitosis as shown in c). **e)** Overlay of quadrilaterals aligned for coordinate $\mathbf{a_2}$ and rotated so that the vector $\mathbf{b_1} - \mathbf{a_2}$ matches the *x*-axis. Control RNAi experiments without manipulation and with ample space in the explant are in black (N = 4), experiments involving manipulation under control RNAi conditions are shown in blue (N = 3), and manipulations experiments under knockdown of Feo are shown in magenta (N = 3). **f)** Quadrilateral area for five different experimental conditions. The same color code as in e) applies; additional control conditions without manipulation in explants almost saturated with nuclei (N = 3) and in explants crowded with nuclei (N = 5) are shown in green and brown, respectively. The dashed line designates the lower boundary where the four nuclei touch each other. **g)** The average mitotic separation distance between the dividing nuclei ($|\mathbf{a_1}–\mathbf{a_2}|$; $|\mathbf{b_1}–\mathbf{b_2}|$) is reduced in the manipulated Feo RNAi condition and is close to the lower limit of separation (nuclear diameter) where the nuclei are touching each other. In contrast, sister nuclei are separated in all the control conditions. The color code is the same as in f). **h)** The average non-sister separation between the dividing nuclei ($|\mathbf{a_1}–\mathbf{b_1}|$; $|\mathbf{a_2}–\mathbf{b_2}|$) is reduced in the manipulated Feo RNAi condition and is close to the lower limit of separation where the nuclei are touching each other. In the control, the distance between the non-sister nuclei is ~25 µm. The color code is the same as in f).

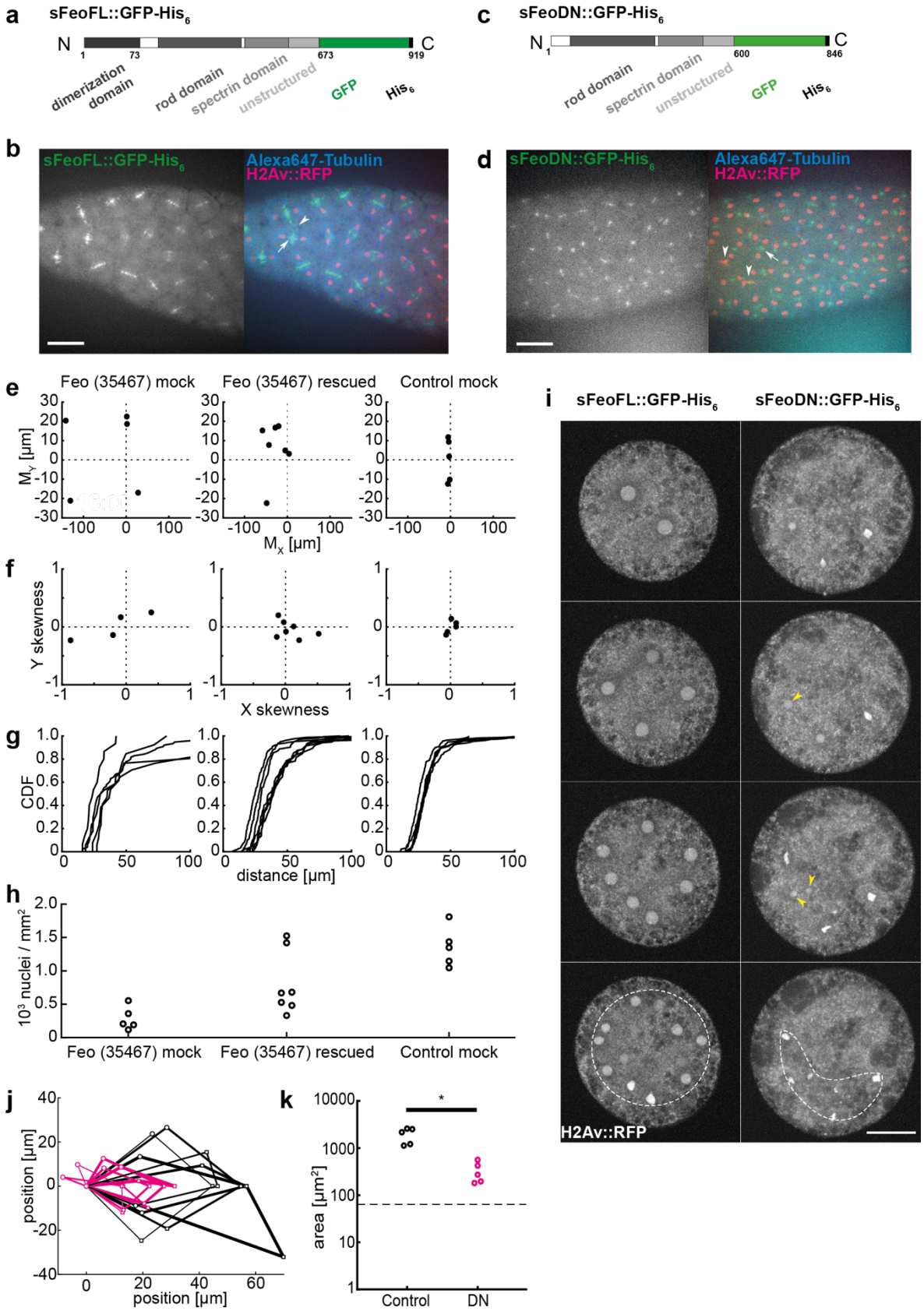

Figure 5: Purified Feo protein rescues nuclear separation in Feo RNAi embryos, and a dominant-negative monomer of Feo abolishes nuclear separation.

863 **a)** Scheme of the synthesized full-length Feo protein fusion construct containing a C-terminal GFP.
864 The domains were determined based on sequence similarity from reported domains of the human
865 construct. The N-terminal end induces dimerization, and the spectrin domain binds to microtubule
866 lattice. **b)** Fluorescence image of the GFP-tagged full-length Feo protein in a blastoderm embryo
867 after protein injection at an earlier stage. The GFP signal alone (left) is shown merged with
868 H2Av::RFP in magenta and Alexa647–Tubulin in blue (right). This Feo construct localizes
869 correctly at the spindle midzone (arrow) and between daughter nuclei (arrowhead) as observed in
870 the transgenic overexpression fly line shown in Fig. 1. Scale bar, 30 µm. **c)** Scheme of a truncated
871 Feo construct lacking the first 73 amino acids of the dimerization domain, fused to a C-terminal
872 GFP. This monomeric protein is a dominant negative (DN) of full length Feo. **d)** Fluorescence
873 image of the GFP-tagged dominant-negative Feo protein in a blastoderm embryo after protein
874 injection at an earlier stage. The GFP signal alone (left) is shown merged with H2Av::RFP in
875 magenta (right). Again, localization at the spindle midzone is observed (arrow). Nuclear separation
876 defects become evident when neighboring nuclei touch or fuse after division (arrowheads). Scale
877 bar, 30 µm. **e)** Plot of the 2-dimensional centroid vector (M_X,M_Y) of all cortical nuclei relative to
878 the embryo center for Feo RNAi embryos either mock injected (left; N = 5) or injected with
879 sFeoFL::GFP-His6 protein (middle; N = 7), compared to mock injected control (mCherry) RNAi
880 embryos (N = 5). The *x*-axis designates the anterior-posterior axis and the *y*-axis is the dorso-ventral
881 axis of the embryo. Deviations from zero mark an acentric delivery of nuclei to the cortex. Along
882 the anterior-posterior axis the injection of Feo full-length protein in Feo RNAi embryos partially
883 rescues centering (middle) while mock-injected Feo RNAi embryos have anatomically eccentric
884 nuclei (left), whereas mock-injected control (mCherry) RNAi embryos exhibit strong centering. **f)**
885 Skewness plot of the positional distribution of all nuclei along the anterior-posterior (*x*) and
886 dorsoventral (*y*) axis for the same conditions as in e). The asymmetric distribution in mock-injected
887 Feo RNAi embryos (left) is partially rescued by Feo protein injection (middle) while mock-injected
888 control embryos show little asymmetry. **g)** Cumulative distribution plot of the first-order neighbor
889 distance between nuclei, for the same conditions as in e) and f). The irregular internuclear distances
890 in mock-injected Feo RNAi embryos (left) are rescued to a considerable extent after full-length
891 protein injection (middle) while mock-injected control (mCherry) RNAi embryos exhibit uniform
892 inter-nuclear distances (right). **h)** The low nuclear density arriving at the cortex in mock-injected
893 Feo RNAi embryos is partially rescued when full-length Feo protein is injected in preblastoderm
894 Feo RNAi embryos. **i)** Addition of full-length Feo::GFP protein to embryo explants expressing
895 H2Av::RFP supports normal nuclear division and regular distribution within the explant space (left,
896 white circle) while addition of dominant-negative Feo protein reduces nuclear separation
897 (arrowheads) and abolishes nuclear distribution (dashed envelope). Scale bar, 30 µm. **j)** Overlay of
898 aligned quadrilaterals describing the nuclear separation after division in explants, as described in
899 Fig. 4. Explants are generated from wildtype embryos and offer ample space for the first few
900 divisions. Experiments involving addition of full-length Feo:GFP protein to the explant are in black
901 (N = 5), experiments involving addition of dominant-negative Feo::GFP protein are shown in
902 magenta (N = 5). **k)** The dominant-negative Feo protein significantly reduces nuclear separation,
903 as measured by the area of quadrilaterals shown in j) when compared to the full-length protein
904 construct (black).

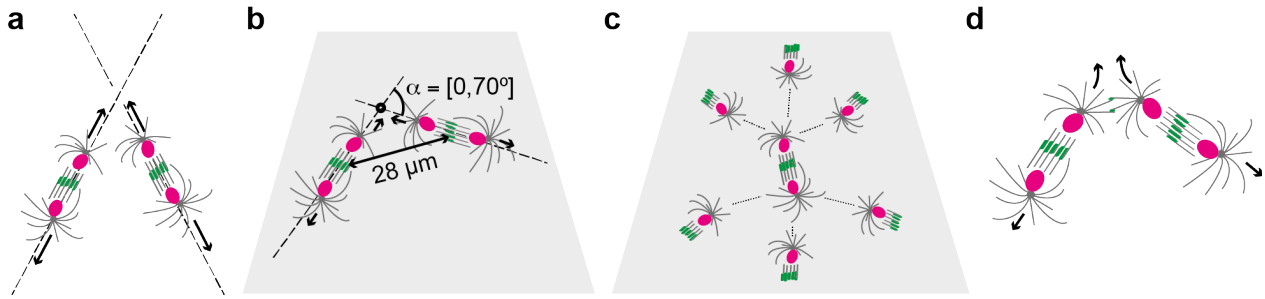

Figure 6: Schematic showing collision trajectories of dividing nuclei in space and on 2-dimensional topologies.

a) Two neighboring spindles with division axes that are oblique. Nuclei separate along the spindle axes, which do not have an intersecting point and do not cause nuclear collision. **b)** Two neighboring spindles with coplanar spindle axes. If these axes are not parallel, they will always form an intersection point. However, because of the short nuclear migration from the previous spindle center (~14 µm), the nuclear diameter (~5 µm) and the average inter-spindle distance (~28 µm), two non-sibling nuclei will only collide if the relative angle alpha between spindle axes is ≤70º. **c)** In a two-dimensional topology of spindles with optimal packing each spindle has six neighbors. In this configuration, and considering the geometric constraints shown in b), no configuration of center spindle axis orientation relative to its neighbors generate a non-sibling nuclear collision. **d)** Model of aster mediated repulsion between neighboring nuclei on a colliding trajectory after mitosis. Astral microtubule crosslinking by Feo and Klp3A generates a repulsive mechanical element that deviates the direction of separating nuclei from the spindle axis.

920 **Supplementary Figures**

921

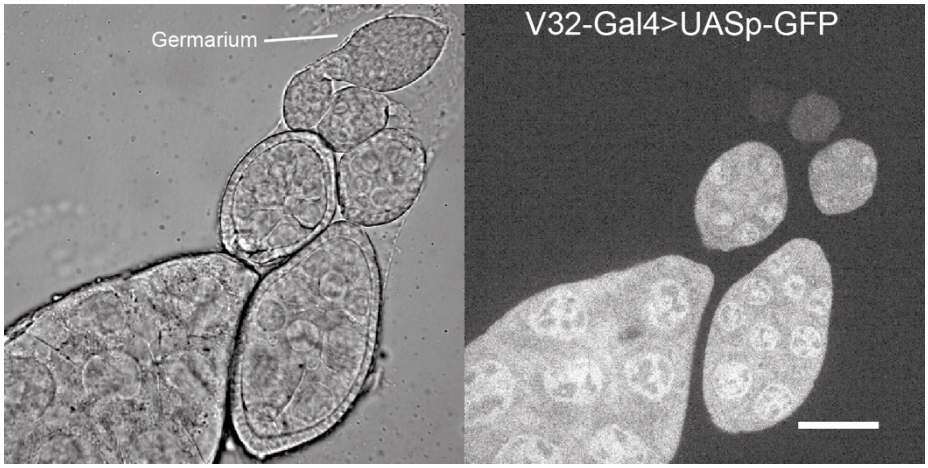

922

923 **Supplementary Figure 1: V32-Gal4 drives expression during late oogenesis.**

924 To evaluate the expression profile of the Gal4 driver, we made a construct expressing V32–Gal4
925 driving UASp–GFP expression specifically in the female germline. The fluorescence intensity in
926 the ovarioles indicates that the peak expression of GFP is achieved only at late stages of oogenesis.
927 It illustrates the expression pattern of UASp constructs under the same Gal4 driver, including the
928 various RNAi constructs described here, with maximum effect in late oogenesis. Scale bar, 10 µm.

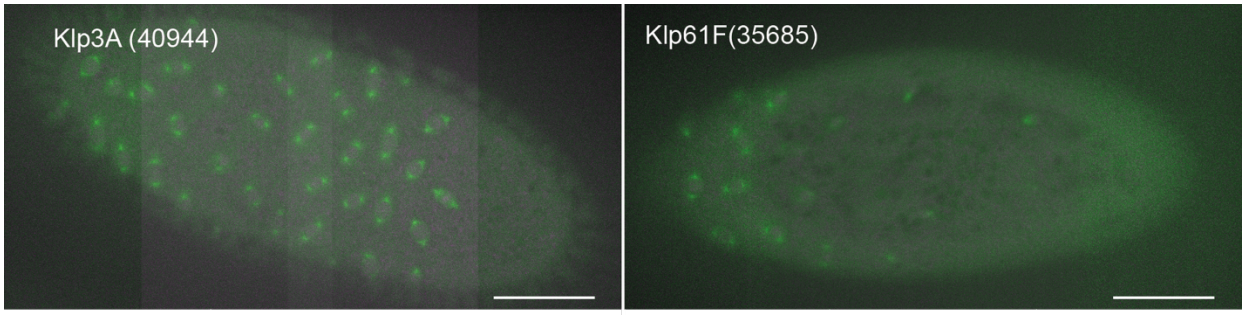

Supplementary Figure 2: Partial knockdown of Klp3A (40944) or Klp61F (33685) by RNAi leads to defective nuclear delivery to the embryo cortex.

Maximum intensity projections from three-dimensional time-lapse movies of embryos partially depleted of Klp3A or Klp61F, expressing Jupiter::GFP (green) marking microtubules and H2Av::RFP (magenta) marking chromatin. These two complementary RNAi lines provide additional support that the knock-down embryos show irregular nuclear distribution during the first interphase occurring at the cortex as compared to the regular nuclear distribution in control embryos (RNAi against mCherry; Fig. 3a). Scale bar, 50 µm.

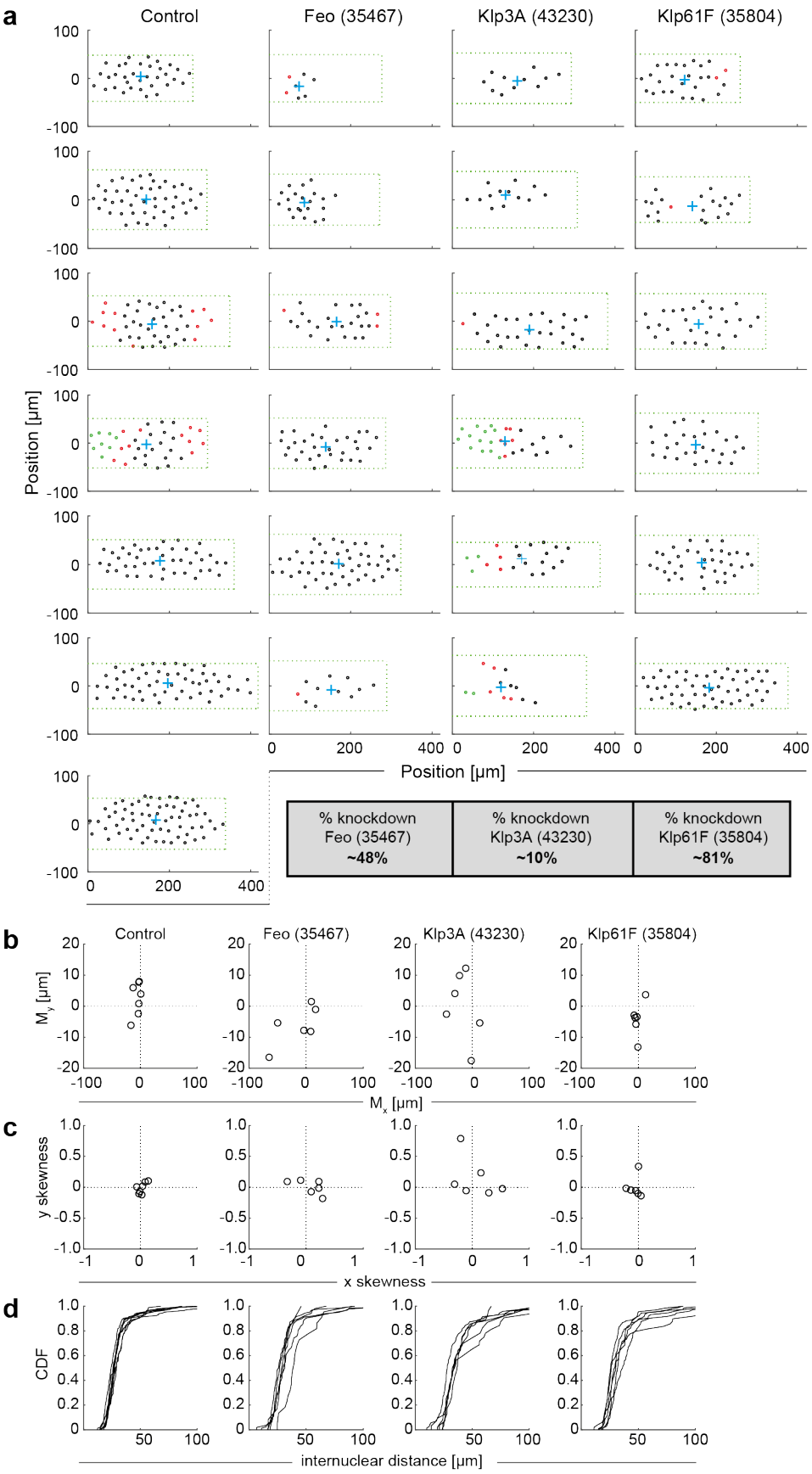

Supplementary Figure 3: Positions of nuclei in each of the analyzed embryos and distribution measurements highlight irregularity in the knockdown constructs.

a) The position (circle) of every nucleus arriving at the embryo cortex after the last preblastoderm division, relative to the axial and lateral borders of the embryo, for each condition – Control (mCherry), Feo (35467), Klp3A (40320), Klp61F (35804). The green dashed rectangle represents the area of the embryo bounded by the length and width of the visible embryo in the confocal stacks, with the anterior end at the coordinate origin. The blue cross represents the location of the 2-dimensional centroid determined from the position of all nuclei. The nuclei in interphase of the first division at the cortex are marked in black, the nuclei that have progressed to metaphase / anaphase are marked in magenta, and the nuclei in telophase / (next) interphase are marked in green. The percent knockdown of mRNA of the lines Feo (35467), Klp3A (40320) and Klp61F (35804) is 48%, 10% and 81%, respectively, as measured by quantitative PCR. **b)** Plot of the 2-dimensional centroid vector (M_x,M_y) of all cortical nuclei relative to the embryo center. The *x*-axis designates the anterior-posterior axis and the *y*-axis is the dorsoventral axis of the embryo. Deviations from zero mark an acentric delivery of nuclei to the cortex. **c)** Skewness plot of the positional distribution of all nuclei along the anterior-posterior (*x*) and dorsoventral (*y*) axis. Feo RNAi and Klp3A RNAi embryos show asymmetric nuclear distribution while nuclei in Klp61F RNAi embryos are distributed symmetrically. **d)** Cumulative distribution plot of the first-order neighbor distance between nuclei. All RNAi lines show higher variability in internuclear distance as compared to the control.

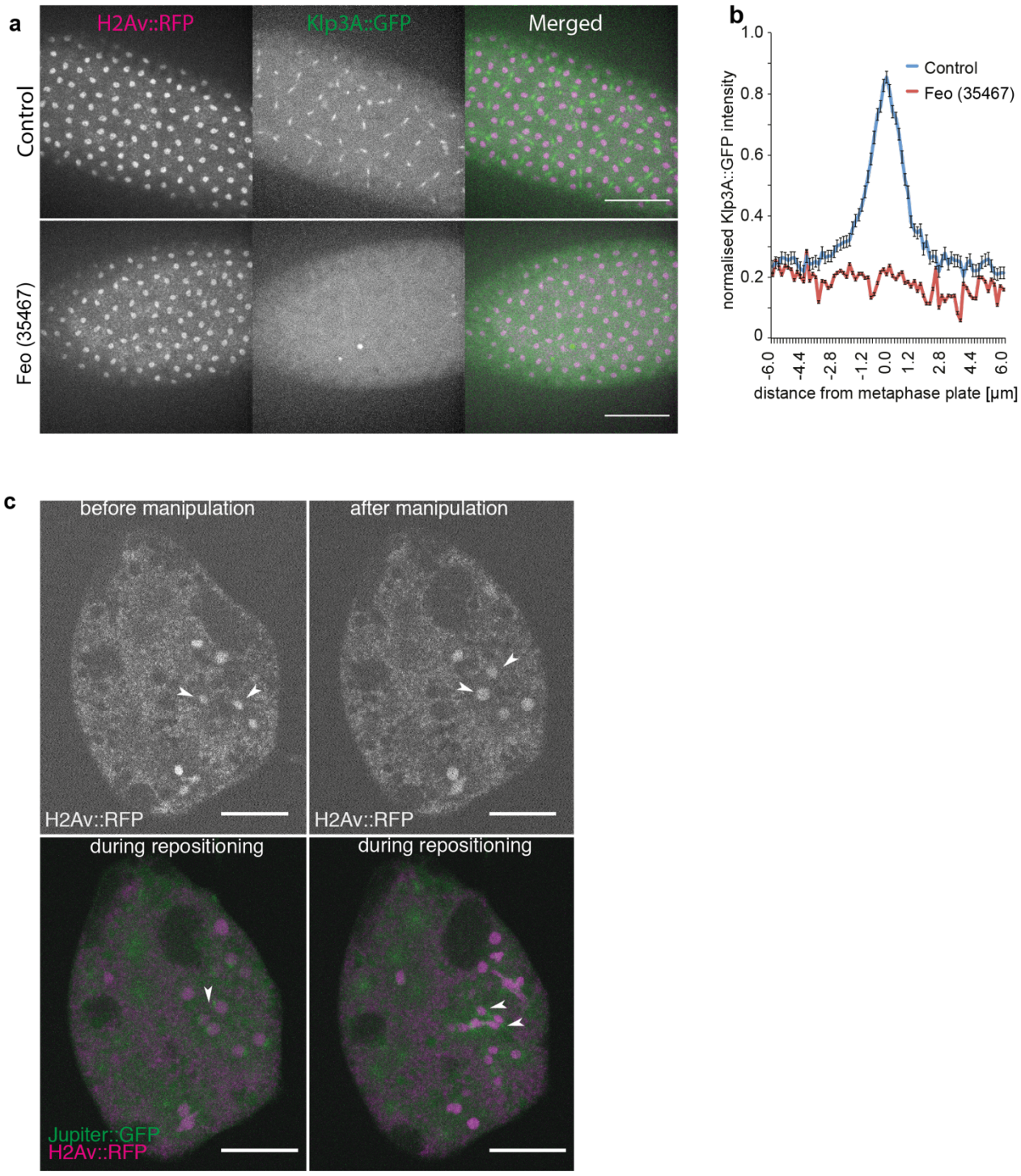

Supplementary Figure 4: Partial depletion of Feo fails to recruit Klp3A to the spindle midzone and does not maintain nuclear separation after manipulation.

a) Snapshots from a time-lapse of embryos expressing H2Av::RFP (magenta, left panel) and Klp3A::GFP (green, middle panel) during anaphase B or telophase. Feo knockdown embryos fail to recruit Klp3A at the spindle midzone when compared to the control embryos expressing no Feo RNAi. **b)** Quantification of Klp3A::GFP intensity measured at the spindle midzone along the spindle axis in control and Feo (35467) embryos. Scale bar, 50 µm. **c)** Physical manipulation of nuclear position in an explant made from an embryo depleted of Feo and expressing Jupiter::GFP

968 (green) marking microtubules and H2Av::RFP (magenta) marking chromatin. After manipulation,
969 the nuclei fail to elicit an efficient repositioning response as observed in the control. Instead, sister
970 and non-sister nuclei fail to separate sufficiently, and nuclei come into contact or form clusters.
971 Scale bar, 30 μm.

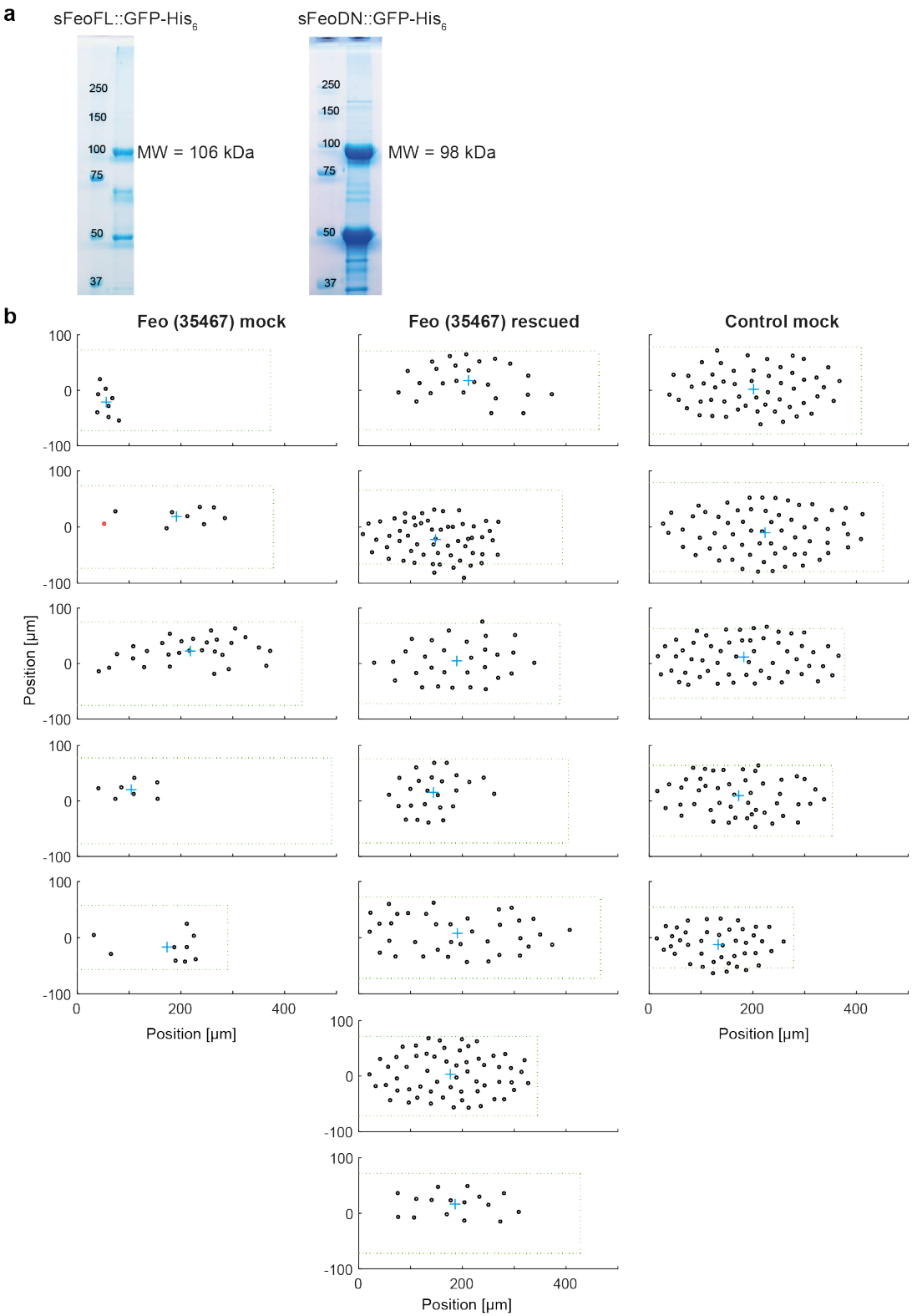

Supplementary Figure 5: Full-length Feo::GFP protein partially rescues nuclear delivery to the cortex of Feo RNAi embryos.

a) Coomassie-stained SDS gel of purified full-length Feo::GFP with an expected molecular weight of 106 kDa (left) and a N-terminally truncated Feo::GFP construct missing the dimerization domain, with expected molecular mass of 98 kDa (right). The lower bands are contaminants that

were not separated by gel filtration and are of bacterial origin as determined by mass spectrometry. **b)** The position (circle) of every nucleus arriving at the embryo cortex after the last preblastoderm division, relative to the axial and lateral borders of the embryo, for each condition: Feo (35467) mock-injected (buffer), Feo (35467) rescued by protein injection, Control (mCherry) mock-injected. The green dashed rectangle represents the area of the embryo bounded by the length and width of the visible embryo in the confocal stacks, with the anterior end at the coordinate origin. The cyan cross represents the location of the 2-dimensional centroid defined from the position of all nuclei. The nuclei in interphase of the first division at the cortex are marked in black, nuclei that have progressed to metaphase / anaphase are marked in magenta.